Stony Brook University

Engineering Interfaces in Polymer/ FullereneBlends

by

Zhenhua Yang

to

The Graduate School

in Partial Fulfillment of the

Requirements

for the Degree of

Doctor of Philosophy

in

Materials Science and Engineering

Stony Brook University

August 2017

Stony Brook University

The Graduate School

Zhenhua Yang

We, the dissertation committee for the above candidate for the

Doctor of Philosophy degree, hereby recommend

acceptance of this dissertation.

Miriam Rafailovich
Dissertation Advisor
Distinguished Professor
Materials Science and Chemical Engineering

T.Venkatesh
Chairperson of Defense
Associate Professor& Graduate Program Director
Materials Science and Chemical Engineering

Chang-Yong Nam
Adjunct Professor
Materials Science and Chemical Engineering

Tai-De Li
Research Assistant Professor
City University of New York, External Member

This dissertation is accepted by the Graduate School

Charles Taber
Dean of *the Graduate* School

Abstract of the Dissertation

Engineering Interfaces in Polymer/ FullereneBlends

by

Zhenhua Yang

Doctor of Philosophy

in

Materials Science and Engineering

Stony Brook University

2017

Polymer fullerene blends have gathered substantial interest in recent years for their potential technological applications, such as optoelectronics and photovoltaics. The performance of these blends is highly dependent on the properties of the nanoparticle-polymer, the polymer-polymer, and the air polymer interfaces. We first investigated the effect of processing additives on the morphology of active layer in polymer solar cell and improved the efficiency by controlling the interface region between active layer and electrode. In particular, polystyrene (PS) with different molecular weights (MW) are used as processing additives in poly[N-9′-heptadecanyl-2,7-carbazole-alt-5,5-(4′,7′-di-2-thienyl-2′,1′,3′-benzothiadiazole)] (PCDTBT)/ phenyl-C61-butyric acid methyl ester (PCBM) solar cell. The interfacial tension between PCDTBT and PS is increased with the increasing PS Mw, which enhances the segregation of the PS phase to the vacuum surface, where the interfacial area is decreased. The migration of PS to the surface mitigated the aggregation of PCBM in the active layer and thus optimized interface region

between active layer and electrode, which led to higher efficiency. Secondly we studied the interfacial interaction between graphene or graphene oxide and poly(methyl methacrylate) (PMMA). The effects of graphene and graphene oxide on the dewetting dynamics of thin polymer films are also investigated. The results indicated that graphene oxide were much more effective than graphene in stabilizing the films against dewetting. The influence of graphene and graphene oxide on the interdiffusion of PMMA films was measured by neutron reflectivity. The diffusion coefficient was unaffected by the presence of graphene but was reduced with graphene, indicating that interactions between the PMMA and graphene were weaker than that between the PMMA and graphene oxide. Finally, eletrospining method is applied to prepare poly[2-methoxy-5-(2-ethylhexyloxy)-1,4-phenylenevinylene] (MEH-PPV)/ polyvinylpyrrolidone (PVP)/PCBM fibers for solar cell devices. By incorporation the fibers into active layer, multipledonor-acceptor interfaces are created in the fibers and in the backfill layer. Compared with the thin-film counterpart, the short-circuit current density and the fill factor are both enhanced in nanofiber-based systems, which is attributed to the favorable morphology provided by the fibrous network serving as a template for the active layer.

Table of Contents

List of Figures

List of Tables

Acknowledgments

First and foremost I would like to express the deepest appreciation and thanks to my advisor, Professor Miriam H. Rafailovich I want first thank my advisor, Prof. Miriam H. Rafailovich, who not only cultivates my research abiltiy, but also excites my deep interests in polymer science. Prof. Rafailovich has the attitude and the substance of a genius: she continually and convincingly converted a spirit of adventure in regard to research and scholarship, and an excitement in regard to teaching. Without her careful guidance, constant encouragement and comprehensive support, I would never be able to finish my PhD program.

I would like to thank my committee members: Prof. T. Venkatesh, Dr. Chang-Yong Nam, and Dr. Tai-De Li for their valuable suggestions and comments. Prof. T. Venkatesh helped me with my PhD class enrollment. Dr. Chang-Yong Nam not only taught me how to prepare a high efficient polymer solar cell device, but also guided me in my research projects. Dr. Tai-De Li from CUNY Advanced Science Research Center helped me with SIMS equipment, which greatly enhanced my understanding on the vertical composition distribution in the polymer thin films.

I also thank Dr. Chung-Chueh Chang, Dr. Ying Liu from Advanced Energy Center and Prof. Guangcui Yuan, Dr Sushil Satjia from National Institute of Standards and Technology for their technical assistance.

I really appreciate the academic communication and support from all the Garia MRSEC members:Dr. Hongfei Li, Dr. Cheng Pan, Dr. Yichen Guo,Dr. Kai Yang, Dr. Yingjie Yu,Dr. Shan He, Dr. Liudi Zhang, Dr. Sisi Qin, Dr. Christine Falabella, Dr. Adriana Sarafova, Dr. Tatsiana Mironava, Dr. NaHyun Cho,Dr. Ke Zhu, Dr.Yan Xu, Yuchen Zhou, Linxi Zhang, Fan Yang, Kuan-Che Feng, Xianghao Zuo,Yuan Xue, Ya-Chen Chuang, Yifan Yin, Clement Marmorat, Vincent Rictta, Kao Li, Juyi Li,Yuval Shmueli and Julia Buassi.

Finally, I would like to thank my family. Without their unconditional love and support, I would not be able to finish my PhD study. I would like to give special thanks to my girlfriend, Lujia Ding, who is always accompanying and encouraging me to conquer all the obstacles on the road.

Chapter 1. Introduction

1.1 Polymer/Fullerene Blend

Fullerenes, the new molecular allotrope of carbon, is among the first places in terms of carbon-based materials in modern material nanoscience.[1] Since they were discovered experimentally for the first time in 1985, fullerenes have attracted increasing attention due to their unique properties[2-4]. Based on those excellent properties, the combination of fullerene with functional polymers has made them candidates for a wide range of applications, such as optical and temperature sensors, photoconductivity, and antimicrobial device.[5-8] In particular, the blends of conjugated polymers and various fullerene derivatives have shown great potential for bulk-heterojunction (BHJ) polymer solar cells and underwent revolutionary growth in the last decade.[9-11] So far, the most widely used fullerene derivativein the BHJ solar cell for the acceptor is Phenyl-C61-butyric acid methyl ester (PCBM) and conjugated polymer for the donor is Poly (3-hexylthiophene) (P3HT). However, the high bandgap of P3HT restricted its absorbance to wavelengths below 650nm and thereby limited further enhancement of the power conversion efficiency(PCE).[12] A great deal of effort has been expended recently to develop low-bandgap polymers, such as Poly[N-9′-heptadecanyl-2,7-carbazole-alt-5,5-(4′,7′-di-2-thienyl-2′,1′,3′-benzothiadiazole)] (PCDTBT), to replace P3HT.[13] The active layer in BHJ solar cell is typically spin coated from the solution of the conjugated polymer and fullerenes and then interconnected domains are formed because of phase separation. With sunlight, the exciton (electron-hole pair) can be generated from the π electrons delocalization in the conjugated polymer in the donor region. And then the excitons will diffuse through the donor phase and dissociate at the interface between the donor and acceptor. Due to the different electron affinities and ionization potentials between the donor and acceptor, the separated free holes will head to the anode of the solar cell along the highest occupied molecular orbital (HOMO) level of the donor and free electrons will forward to the cathode through the accepters lowest unoccupied molecular orbital (LUMO) level. Therefore, the current will be created in the external circuit of the BHJ solar cell by collecting the electrons and holes at corresponding electrode.[14-16]

Morphology control in BHJ solar cell is an essential consideration for enhancing the power conversion efficiency (PCE). Earlier studies have attempted to optimize the morphology of the active layer with different methods including thermal annealing, components ratio adjustment, and processing additives.[17-19] Among those methods, adding processing additive is the simplest and fastest way for morphology optimization because this method only requires the incorporation of a small amount of the processing additives into the polymer and fullerene blend solution without any post-treatment.[20]

Even though the efficiencies of BHJ solar cells have been improved by different additives, such as poly(N-(4-(9,9-dioctyl-fluoren-2-yl)phenyl)-N,N′,N′-triphenyl-l,4-phenylenediamine) (PFLAM) and poly(oxyethylene tridecyl ether) (PTE),[12, 20] the interaction between additives and polymer donor, especially the interface properties, has not been fully understood. Here, we show how polystyrene (PS) can be used as a processing additive to enhance the performance of PCDTBT/PCBM BHJ solar cell device through increasing the crystallinity of the polymer donor. This enhancement in efficiency is correlated with the interface properties between PS and PCDTBT including interfacial tension and interfacial width.

As a 2D monolayer of carbon crystal with similar honeycomb lattice in fullerene, graphene and graphene derivatives such as graphene oxide (GO), have also been an area of intense interest in recent years owing to its exceptionally unique electronic and optical properties.[21-26] Graphene and GO are usually used as functional nanofiller for improving mechanical, electrical, thermal, and gas barrier performance of polymers.[27-31] Although considerable research has been devoted to studying the improved properties and compatibilization effect of graphene and GO in bulk polymer-blend nanocomposites,[32, 33] little attention has been paid to the dynamics and morphology of graphene and GO doped polymer thin films. Polymer thin films exhibit different physical properties compared with bulk polymers due to that the confinement effect in thin films affects the dynamic properties and wetting characteristics.[34] Polymer thin films have been shown to be increasingly important because of their indispensable role in applications such as protective coatings, lubricants, decorative paints, adhesives, biomembranes, sensors, as active layers in devices such as organic light-emitting diodes (OLED), organic field effect transistors (OFET),

organic solar cells and organic laser devices, and to modify surface wettabilities.[35-41] However, a persistent concern with polymer thin films is their stability against dewetting, which is caused by the unfavorable interfacial tension between most polymers.[42] We here show that the dewetting can be controlled by adding graphene and GO into polymer thin films due to the favorable interactions of the polymer with the nanofillers.

Electrospinning is a well-established and straightforward technique for the realization of continuous fibers with diameters ranging from tens of nanometers to several micrometers through the application of a high voltage bias to polymer solutions.[43, 44] This process allows the production of an entangled nonwoven fiber network with high surface-area-to-volume ratio, which can be deposited in random networks or in uniaxially aligned arrays with three-dimensional porosity. Due to its versatility in terms of usable polymers and blends, electrospinning shows high potential as a method to tailor the microstructure and the composition of active materials for polymer optoelectronic devices such as polymer solar cells[45]. However, electrospinning conjugated polymers with fullerenes is frequently difficult due to the generally poor viscoelastic behavior of the solutions.[46-49] Here we report a simple method to facilitate the electrospinning process by using polymer blend of poly[2-methoxy-5-(2-ethylhexyloxy)-1,4 phenylenevinylene]/polyvinylpyrrolidone/PCBM (MEH-PPV/PVP/PCBM). The resulted nanofibers are stable, easily produced, and yet photoactive, and can also improve the performance of BHJ solar cells when incorporated into the active layer.

1.2 Outline of Chapters

In Chapter 2, we show how the efficiency of PCDTBT/PCBM blends can be enhanced via the addition of small volume fractions of PS and we directly establish a correlation between the interfacial tension between the polymer components and the efficiency. We also explore the influence of PS with different molecular weight on the compositional gradient in the vertical direction for PCDTBT/PCBM inverted solar cell. With high molecular weight PS, the devices show a great increment in efficiency resulted from optimized compositional gradient in the vertical direction.

In Chapter 3, we have investigated the effect of graphene and GO on the long-ranged motion and chain dynamics of polymer thin films. In the dewetting experiment where long-ranged motion occurs, GO is more effective than graphene at stabilizing the polymer films against dewetting. The same trend was also observed for the single chain dynamics of poly(methyl methacrylate) (PMMA) film. The tracer diffusion coefficient was reduced by addition of GO while it was unaffected by the presence of the graphene nanoparticles. Those effects are caused by the more favorable interaction of GO with the polymer thin film.

In Chapter 4, we showed that MEH-PPV/PVP/PCBM nanofibers can be successfully prepared via electrospinning and incorporated into the active layer of polymer solar cell devices. The entangled fiber network serves as a template for the active layer, with effects promoting diffusion and dissociation of photogenerated excitons at involved organic interfaces as well as light-scattering redirecting incident photons across active layers. The resulting devices are found to exhibit improved efficiency compared to the control device without nanofibers.

Reference

1. Dinadayalane, T. C.; Leszczynski, J. Remarkable diversity of carbon-carbon bonds: structures and properties of fullerenes, carbon nanotubes, and graphene. *Struct. Chem.* 2010, 21, 1155-1169.

2. Zhang, N.; Zhang, Y. H.; Yang, M. Q.; Tang, Z. R.; Xu, Y. J. A critical and benchmark comparison on graphene-, carbon nanotube-, and fullerene-semiconductor nanocomposites as visible light photocatalysts for selective oxidation. *J. Catal.* 2013, 299, 210-221.

3. Hino, T.; Ogawa, Y.; Kuramoto, N. Preparation of functionalized and non-functionalized fullerene thin films on ITO glasses and the application to a counter electrode in a dye-sensitized solar cell. *Carbon* 2006, 44, 880-887.

4. Kanbara, T.; Shibata, K.; Fujiki, S.; Kubozono, Y.; Kashino, S.; Urisu, T.; Sakai, M.; Fujiwara, A.; Kumashiro, R.; Tanigaki, K. N-channel field effect transistors with fullerene thin films and their application to a logic gate circuit. *Chem. Phys. Lett.* 2003, 379, 223-229.

5. Kausar, A. Advances in Polymer/Fullerene Nanocomposite: A Review on Essential Features and Applications. *Polym-Plast Technol* 2017, 56, 594-605.

6. Sweetnam, S.; Vandewal, K.; Cho, E.; Risko, C.; Coropceanu, V.; Salleo, A.; Bredas, J. L.; McGehee, M. D. Characterizing the Polymer:Fullerene Intermolecular Interactions. *Chem. Mater.* 2016, 28, 1446-1452.

7. Hong, S. W.; Kim, D. Y.; Lee, J. U.; Jo, W. H. Synthesis of Polymeric Temperature Sensor Based on Photophysical Property of Fullerene and Thermal Sensitivity of Poly(N-isopropylacrylamide). *Macromolecules* 2009, 42, 2756-2761.

8. Yakuphanoglu, F. Photovoltaic properties of the organic-inorganic photodiode based on polymer and fullerene blend for optical sensors. *Sensor Actuat a-Phys* 2008, 141, 383-389.

9. Zhang, F. L.; Inganas, O.; Zhou, Y. H.; Vandewal, K. Development of polymer-fullerene solar cells. *Natl Sci Rev* 2016, 3, 222-239.

10. Lu, L. Y.; Zheng, T. Y.; Wu, Q. H.; Schneider, A. M.; Zhao, D. L.; Yu, L. P. Recent Advances in Bulk Heterojunction Polymer Solar Cells. *Chem. Rev.* 2015, 115, 12666-12731.

11. Dou, L. T.; You, J. B.; Hong, Z. R.; Xu, Z.; Li, G.; Street, R. A.; Yang, Y. 25th Anniversary Article: A Decade of Organic/Polymeric Photovoltaic Research. *Adv. Mater.* 2013, 25, 6642-6671.

12. Huh, Y. H.; Park, B. Interface-engineering additives of poly(oxyethylene tridecyl ether) for low-band gap polymer solar cells consisting of PCDTBT:PCBM70 bulk-heterojunction layers. *Opt. Express* 2013, 21, A146-A156.

13. Chu, T. Y.; Alem, S.; Verly, P. G.; Wakim, S.; Lu, J. P.; Tao, Y.; Beaupre, S.; Leclerc, M.; Belanger, F.; Desilets, D.; Rodman, S.; Waller, D.; Gaudiana, R. Highly efficient polycarbazole-based organic photovoltaic devices. *Appl. Phys. Lett.* 2009, 95.

14. Yu, G.; Gao, J.; Hummelen, J. C.; Wudl, F.; Heeger, A. J. Polymer Photovoltaic Cells - Enhanced Efficiencies Via a Network of Internal Donor-Acceptor Heterojunctions. *Science* 1995, 270, 1789-1791.

15. Hoppe, H.; Sariciftci, N. S. Organic solar cells: An overview. *J. Mater. Res.* 2004, 19, 1924-1945.

16. Scharber, M. C.; Wuhlbacher, D.; Koppe, M.; Denk, P.; Waldauf, C.; Heeger, A. J.; Brabec, C. L. Design rules for donors in bulk-heterojunction solar cells - Towards 10 % energy-conversion efficiency. *Adv. Mater.* 2006, 18, 789-+.

17. Al-Ibrahim, M.; Ambacher, O.; Sensfuss, S.; Gobsch, G. Effects of solvent and annealing on the improved performance of solar cells based on poly(3-hexylthiophene): Fullerene. *Appl. Phys. Lett.* 2005, 86.

18. Liao, H. C.; Ho, C. C.; Chang, C. Y.; Jao, M. H.; Darling, S. B.; Su, W. F. Additives for morphology control in high-efficiency organic solar cells. *Mater. Today* 2013, 16, 326-336.

19. Lee, T. H.; Park, S. Y.; Walker, B.; Ko, S. J.; Heo, J.; Woo, H. Y.; Choi, H.; Kim, J. Y. A universal processing additive for high-performance polymer solar cells. *RSC Adv.* 2017, 7, 7476-7482.

20. Chen, M. C.; Liaw, D. J.; Chen, W. H.; Huang, Y. C.; Sharma, J.; Tai, Y. Improving the efficiency of an organic solar cell by a polymer additive to optimize the charge carriers mobility. *Appl. Phys. Lett.* 2011, 99.

21. Umeyama, T.; Baek, J.; Tezuka, N.; Morita, K.; Imahori, H. Incorporation of Graphene to Fullerene Clusters and Fullerene-Nanotube Composites and Their Photoelectrochemical Properties. *Ecs J Solid State Sc* 2013, 2, M3001-M3007.

22. Novoselov, K. S.; Geim, A. K.; Morozov, S. V.; Jiang, D.; Zhang, Y.; Dubonos, S. V.; Grigorieva, I. V.; Firsov, A. A. Electric field effect in atomically thin carbon films. *Science* 2004, 306, 666-669.

23. Geim, A. K.; Novoselov, K. S. The rise of graphene. *Nat. Mater.* 2007, 6, 183-191.

24. Allen, M. J.; Tung, V. C.; Kaner, R. B. Honeycomb Carbon: A Review of Graphene. *Chem. Rev.* 2010, 110, 132-145.

25. Novoselov, K. S.; Geim, A. K.; Morozov, S. V.; Jiang, D.; Katsnelson, M. I.; Grigorieva, I. V.; Dubonos, S. V.; Firsov, A. A. Two-dimensional gas of massless Dirac fermions in graphene. *Nature* 2005, 438, 197-200.

26. Zhang, Y. B.; Tan, Y. W.; Stormer, H. L.; Kim, P. Experimental observation of the quantum Hall effect and Berry's phase in graphene. *Nature* 2005, 438, 201-204.

27. Pham, V. H.; Dang, T. T.; Hur, S. H.; Kim, E. J.; Chung, J. S. Highly Conductive Poly(methyl methacrylate) (PMMA)-Reduced Graphene Oxide Composite Prepared by Self-Assembly of PMMA Latex and Graphene Oxide through Electrostatic Interaction. *ACS Appl. Mater. Interfaces* 2012, 4, 2630-2636.

28. Kim, H.; Abdala, A. A.; Macosko, C. W. Graphene/Polymer Nanocomposites. *Macromolecules* 2010, 43, 6515-6530.

29. Kuilla, T.; Bhadra, S.; Yao, D. H.; Kim, N. H.; Bose, S.; Lee, J. H. Recent advances in graphene based polymer composites. *Prog. Polym. Sci.* 2010, 35, 1350-1375.

30. Potts, J. R.; Dreyer, D. R.; Bielawski, C. W.; Ruoff, R. S. Graphene-based polymer nanocomposites. *Polymer* 2011, 52, 5-25.

31. Bai, H.; Li, C.; Shi, G. Q. Functional Composite Materials Based on Chemically Converted Graphene. *Adv. Mater.* 2011, 23, 1089-1115.

32. You, F.; Wang, D. R.; Li, X. X.; Liu, M. J.; Dang, Z. M.; Hu, G. H. Synthesis of Polypropylene- Grafted Graphene and Its Compatibilization Effect on Polypropylene/ Polystyrene Blends. *J. Appl. Polym. Sci.* 2014, 131.

33. Cao, Y. W.; Zhang, J.; Feng, J. C.; Wu, P. Y. Compatibilization of Immiscible Polymer Blends Using Graphene Oxide Sheets. *ACS Nano* 2011, 5, 5920-5927.

34. Reiter, G.; Schultz, J.; Auroy, P.; Auvray, L. Improving adhesion via connector polymers to stabilize non-wetting liquid films. *Europhys. Lett.* 1996, 33, 29-34.

35. Xue, L. J.; Han, Y. C. Inhibition of dewetting of thin polymer films. *Prog. Mater Sci.* 2012, 57, 947-979.

36. Bandyopadhyay, D.; Douglas, J. F.; Karim, A. Influence of C-60 Nanoparticles on the Stability and Morphology of Miscible Polymer Blend Films. *Macromolecules* 2011, 44, 8136-8142.

37. Cowie, J. M. G. *Polymers: chemistry and physics of modern materials*.

38. Singh, J.; Agrawal, K. K. Polymeric Materials for Contact-Lenses. *J Macromol Sci R M C* 1992, C32, 521-534.

39. Helgesen, M.; Sondergaard, R.; Krebs, F. C. Advanced materials and processes for polymer solar cell devices. *J. Mater. Chem.* 2010, 20, 36-60.

40. Lu, G.; Usta, H.; Risko, C.; Wang, L.; Facchetti, A.; Ratner, M. A.; Marks, T. J. Synthesis, characterization, and transistor response of semiconducting silole polymers with substantial hole mobility and air stability. Experiment and theory. *J. Am. Chem. Soc.* 2008, 130, 7670-7685.

41. Armstrong, N. R.; Wang, W. N.; Alloway, D. M.; Placencia, D.; Ratcliff, E.; Brumbach, M. Organic/Organic' Heterojunctions: Organic Light Emitting Diodes and Organic Photovoltaic Devices. *Macromol. Rapid Commun.* 2009, 30, 717-731.

42. Wyart, F. B.; Martin, P.; Redon, C. Liquid-Liquid Dewetting. *Langmuir* 1993, 9, 3682-3690.

43. Li, D.; Xia, Y. N. Electrospinning of nanofibers: Reinventing the wheel? *Adv. Mater.* 2004, 16, 1151-1170.

44. Agarwal, S.; Greiner, A.; Wendorff, J. H. Electrospinning of Manmade and Biopolymer Nanofibers-Progress in Techniques, Materials, and Applications. *Adv. Funct. Mater.* 2009, 19, 2863-2879.

45. Persano, L.; Camposeo, A.; Pisignano, D. Active polymer nanofibers for photonics, electronics, energy generation and micromechanics. *Prog. Polym. Sci.* 2015, 43, 48-95.

46. Kim, T.; Yang, S. J.; Kim, S. K.; Choi, H. S.; Park, C. R. Preparation of PCDTBT nanofibers with a diameter of 20 nm and their application to air-processed organic solar cells. *Nanoscale* 2014, 6, 2847-2854.

47. Bedford, N. M.; Dickerson, M. B.; Drummy, L. F.; Koerner, H.; Singh, K. M.; Vasudev, M. C.; Durstock, M. F.; Naik, R. R.; Steckl, A. J. Nanofiber-Based Bulk-Heterojunction Organic Solar Cells Using Coaxial Electrospinning. *Adv. Energy. Mater.* 2012, 2, 1136-1144.

48. Kim, T.; Yang, S. J.; Sung, S. J.; Kim, Y. S.; Chang, M. S.; Jung, H.; Park, C. R. Highly Reproducible Thermocontrolled Electrospun Fiber Based Organic Photovoltaic Devices. *ACS Appl. Mater. Interfaces* 2015, 7, 4481-4487.

49. Kim, M.; Jo, S. B.; Park, J. H.; Cho, K. Flexible lateral organic solar cells with core-shell structured organic nanofibers. *Nano Energy* 2015, 18, 97-108.

Chapter 2.Enhancing the Efficiency of Bulk Heterojunction Solar Cell with Processing Additive

2.1 Introduction

Bulk heterojunction (BHJ) solar cells have been extensively studied due to their flexibility and the potential to enable high-throughput roll-to-roll fabrication.[1-4]Recently, Most of the high-efficiency polymer:fullerene solar cells have adopted an inverted-type device structure, in which metal oxides such as titanium oxide or zinc oxide (ZnO) are used as the charge-collecting buffer layer instead of the corrosive and hygroscopic hole-transporting poly(3,4-ethylenedioxylenethiophene):poly(styrenesulphonic acid) (PEDOT:PSS).[5-10] By avoiding the need for PEDOT:PSS and low-work-function metal cathode, inverted- type devices achieve better long-term ambient stability than normal-type devices.[11, 12]

Morphology control of the active layer in BHJ solar cellshas been shown to be an essential consideration that could improve the power conversion efficiency (PCE).[13] The active layer of the BHJ usually consists of an interpenetrating network of electron- donating conjugated polymers and electron-accepting fullerenes.[14]The miscibility of the donor and acceptor materials, the size and composition of the phase-separated domains, their crystalline character, the presence of percolating charge transportnetworks, and the vertical concentration gradient are all important factors that must be considered when optimizing the morphology of the BHJ active layer.[15-19]In particular, The use of BHJ with favorable compositional gradient in the vertical direction to establish charge selectivity at the electrode have been proposed as an effective approach to enhance the efficiency of polymer solar cell, regardless of the types of polymer donor and electron acceptor.[20-22] For example, the preferential segregation of the polymer donorto the anode-active layer interface can block electrons and enhance hole collection, which would lead to enhanced short circuit current density and improved device performance. Conversely, preferential segregation of fullerene to the anode-active layer interfacecould dramatically increase the seriesresistance and block the hole transportation, resulting in decreased device performance.[23] Segregation of the electron acceptor phase can be controlled within the blend by

the addition of a tertiary component. Pan .et al and Li .et al have shown that addition of a third component could lead to the formation of columns within the films which can template the PCBM, thereby shortening the pathway to the electrodes and decreasing the recombination rate. [13, 24]This method though introduced large volume fractions of an inert component, which decreased the photoconversion of the films.

Sun et al have shown that the addition of small amounts of block copolymers as the tertiary phase in a poly(3-hexylthiophene-2,5-diyl) (P3HT) and phenyl-C61-butyric acid methyl ester (PCBM) blend can decrease the interfacial tension and prevent layering due to phase segregation within the film. This method was shown to significantly increase the efficiency of devices since it minimized the volume of the inert phase while preventing the obstruction of charge carriers reaching the respective electrodes.[25]However, the high bandgap of P3HT restricted its absorbance to wavelengths below 650nm andtherebylimited further enhancement of the PCE.[26]A great deal of effort has been expended recently to develop low-bandgap polymers, such as poly[N-9′-heptadecanyl-2,7-carbazole-alt-5,5-(4′,7′-di-2-thienyl-2′,1′,3′-benzothiadiazole)] (PCDTBT), to replace P3HT.[27]However, since the interfacial energies between PCDTBT and PCBM are very different from those in the P3HT/PCBM blends, the internal morphology of the films is also very different, and new approaches must be developed in order to find the structures that optimize the efficiency. In contrast to P3HT, PCDTBT is far more compatible with other polymers making it more difficult to achieve a phase segregated morphology and requiring a much larger volume fraction of PCBM to achieve percolation. In this blend therefore, the challenge is to increase immiscibility, and sharpen interfacial contrast, while at the same time preventing layering. Hence the approaches which increased the efficiency of P3HT/PCBM blends would not work in this case since they were based on reduction of the interfacial tension, rather increasing it.

It is well established that immiscibility between polymers can be enhanced with increasing molecular weight.[28]Therefore in this chapterwe show how the efficiency of PCDTBT /PCBM blends can be enhanced via the addition of small volume fractions of high molecular weight monodispersed polymers and we directly establish a correlation between the interfacial tension between the polymer components and the efficiency. Weexplore the influence of processing

additives on the compositional gradient in the vertical direction for PCDTBT/PCBM inverted solar cell. High molecular weight polystyrene (PS) was used as a processing agent to control the vertical components distribution of the active layer. We extend the previously studies on lateral morphology through probingchemical composition distribution verticallywith SIMS and WAXS. The photovoltaic properties of devices are correlated with the vertical components distribution in the active layer. Upon only a small amount of PS, the devices show a great increment in efficiency resulted from optimized compositional gradient in the vertical direction. We believe that this study will contribute to optimizing the morphology for other electron donor–electron acceptor pairs and lead to improved device performance for those systems.

2.2 Experiment

2.2.1 Materials

PCDTBT was purchased from 1-material Company. PCBM is provided by SES research. Chlorobenzene is obtained from Sigma-Aldrich. PS with different molecular weight was purchased from Polymer source. All materials are used without further purification.

2.2.2 Device Fabrication

Indium tin oxide (ITO)-coated glass slide was polished in UV ozone for 10 min. TiO_2 solution was synthesized according to previous report.[29]A 30 nm thick TiO_2 layer was spun-cast onto the ITO glass at 3000 rpm for 20 s and was baked at 400 °C for 2h on the hot plate exposed to the air. Chlorobenzene solution composed of PS/PCDTBT/PCBM was spin-cast at 3000 rpm for 45s on top of TiO_2 layer in atmosphere. The typical film thickness of active layer is around 100 nm. Then the samples were annealed in vacuum oven at 150 °C for 10 min. Finally, the devices were completed by thermal evaporation of 8 nm MoO_3 and 100 nm Ag electrode with the help of Kurt J. Lesker PVD 75 vacuum deposition systems at Brookhaven National Laboratory.

2.2.3 Sample Characterization

Device Characterization: The performance of solar cell device was tested by a 150 W solar simulator (Oriel) with an AM 1.5G filter for solar illumination. The light intensity was calibrated to 100 mW cm^{-2} by a calibrated thermopile detector (Oriel). UV-vis absorption spectroscopy was carried by a Thermo Scientific Evolution 200 UV-VIS Spectrophotometer. Images of the surface topography were obtained using a Bruker Dimension Icon atomic force microscope (AFM) (Multimode, Bruker) operating in contact mode.

SCLC Mobility Measurement: The hole-only diodes and electron-only diodes were fabricated for SCLC mobility measurement. The devices geometry similar to solar cell devices, except that TiO_2 was replaced by PEDOT:PSS for hole-only diodes while MoO_3/Ag was substituted by Al for electron-only diodes. The J–V characteristics of the diodes were fitted with the Mott–Gurney equation for space charge limited current (SCLC): $J = 9\varepsilon_r\varepsilon_0\mu V^2 /8L^3$, where ε_r is the relative dielectric constant, ε_0 the permittivity of free space, μ the zero-field mobility and L the active layer thickness.

GIWAXS measurement: GIWAXS measurements for the PCDTBT/PCBM blend films were carried out at the 8-ID-E beamline (λ = 0.11363 nm and E = 10.91 keV) at the Advanced Photon Source (APS), Argonne National Laboratory. The experiment is conducted with two different mode:(i) incident angle (α= 0.12°) is just below the critical angle (α_c) of the total external reflection for PCDTBT such that the electric field intensity decays exponentially into the film, and therefore the scattering intensity is dominated by the surface area of 10 nm depth; (ii) incident angle (α= 0.14°) is just above the critical angle (α_c), where we can obtain information on the average structures over the entire film. All samples were measured at room temperature under vacuum.

SIMS measurement: The depth profiles of the blend films on SiO_2 / Si substrateswere obtained with a PHI TRIFT V nanoTOF SIMS at the City University of New York Advanced Science

Research Center. A 20 kV Gas Cluster Ion Beam (GCIB) with Ar^+at ca. 6 nA was rastered across a 300 μm x300 μm area, of which only the middle 10% was analyzed for composition by collecting negative secondary ions. The films were prepared by spun cast blends solutions atop of SiO_2 /Si substrate using the same processing parameters for solar cell devices. The signal for the PCBM comes from $^{16}O^-$ while the $^2H^-$ signal represents the deuterium polystyrene (d-PS) component.The Si and carbon signal is collected for determining the end point of film. The typical depth profile is shown in figure 2.1, in which the small oxygen peak with width of 3nm at near depth of 90 nm represents the thin SiO_2layer. The appearance of this peak indicates the finishing line of blend film.

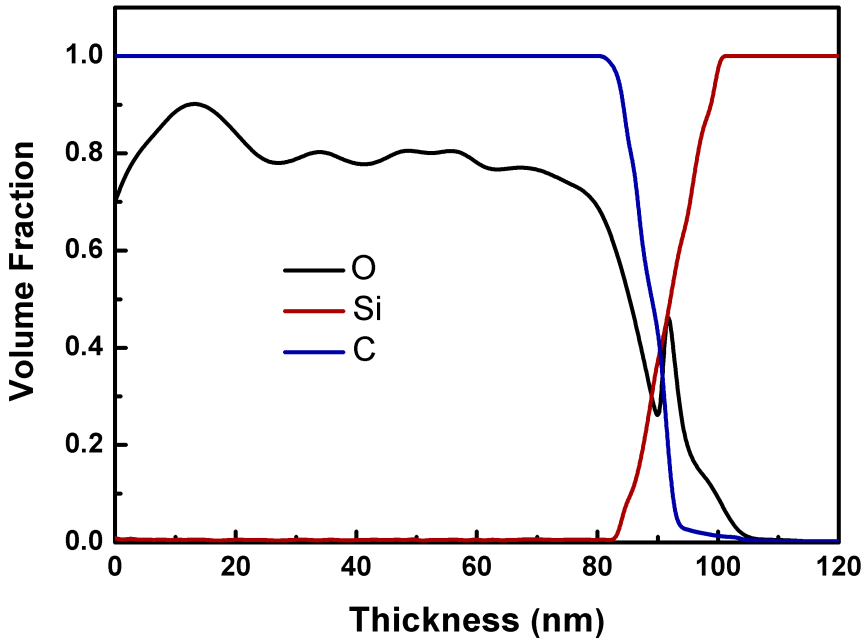

Figure 2. 1SIMS profiles for the composition volume fraction in PCDTBT:PCBM blends film on Si substrate

2.3Results and Discussion

2.3.1 Device Performance

Pan et al[13]as well as Vohra et al[30]have shown that the efficiency of BHJ solar cells could be increased by adding a tertiary photo inert componentPS, in a concentration of 1:1 with P3HT. In their case it was postulated that the third component would template the PCBM, shorten the path length to the conductors,[13]and nucleate crystal structure.[30]Ade et al[31]added only a few percent of PS to a blend of small molecular weight photoactive polymer and also achieved enhanced performance, even though the PS concentration was too low for the formation of columns. The volume fraction of polymer with face on crystalline orientation was significantly increased.

In order to understand the mechanism responsible in greater depth, and whether it was also applicable to long chain photovoltaic polymers, we explored the role of molecular weight and concentration on the PS:PCDTBT system.In figure 2.2a we show the current density–voltage characteristics for a device made from a blend of PCDTBT:PS:PCBM where the PS had a Mw=2M. The fitting parameters for the curves for various concentrations of PS are given in table 2.1 and the efficiency is plotted as a function of concentration in figure 2.2b. From the figure we find that there is a distinct peak in the concentration around 2.5%, or roughly the same weight percent as that reported by Ade.[31]Hence in this system of high molecular weight polymers, enhancement can be achieved without formation of columnar internal structures, which is a distinct advantage, since less volume is occupied by the photo-inertcomponent.

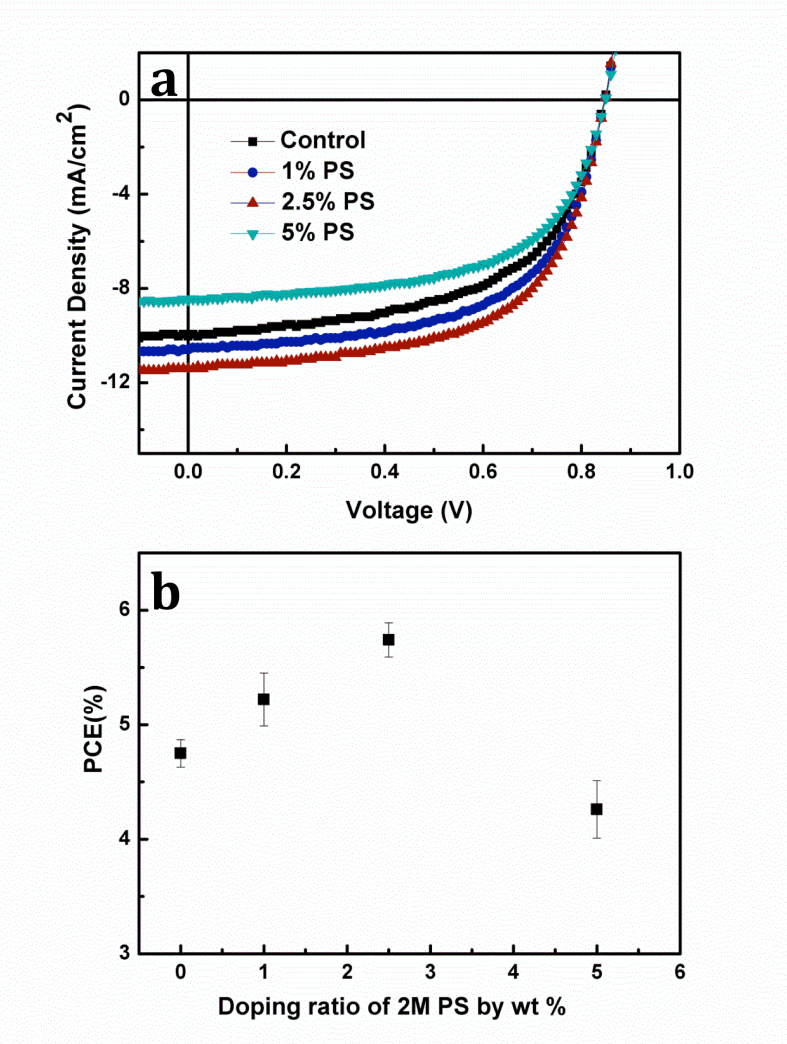

Figure 2. 2 (a) Current density–voltage (J–V) characteristics of BHJ devices based on PCDTBT:PCBM with different doping ratio of PS; (b) the device efficiency with different PS doping ratio

PCDTBT:PCBM	Jsc(mA/cm2)	Voc(V)	FF	PCE(%)
Control	10.02±0.3	0.84±0.01	0.57±0.02	4.75±0.12
1 wt% PS	10.57±0.5	0.84±0.02	0.59±0.03	5.22±0.23
2.5 wt% PS	11.25±0.4	0.85±0.01	0.60±0.02	5.74±0.15
5 wt% PS	8.59±0.3	0.84±0.01	0.59±0.02	4.26±0.25

Table 2. 1 Device parameters of BHJ devices based on PCDTBT:PCBM with different doping ratio of 2M PS

In order to explore this mechanism in greater detail, we then measured the efficiency as a function of molecular weight, at a fixed volume fraction of 2.5%. The current density–voltage cruvesfor this set of experiments are shown in figure 2.4, and the fitting parameters are tabulated in table 2.3. The efficiency is plotted as a function of molecular weight in figure 2.6d where we see that initially for the lower molecular weights starting atMw=50K, the efficiency is decreased relative to the control sample, but as the PS molecular weight increases, it climbs above the value for the control device, reaching a plateau in the region of Mw=2M to at least Mw=7M, with a total enhancement exceeding 20%. It should be noted though the PS concentration in each case was kept fixed at 2.5%. Increasing the concentration to 20%, as would be required for the formation of columns decreased the efficiency (figure2.3 and table 2.2).

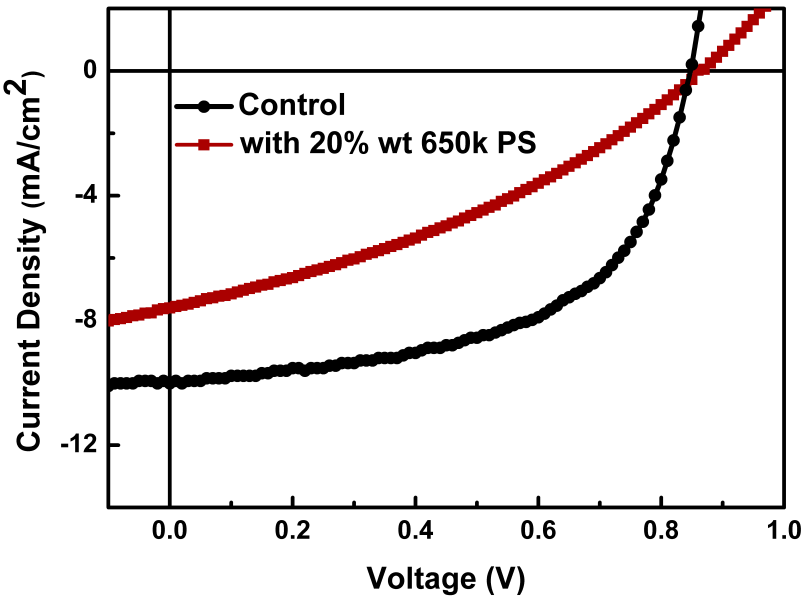

Figure 2. 3 The efficiency of BHJ devices based on PCDTBT:PCBM with and without 20%wt 650k PS

PCDTBT:PCBM	Jsc(mA/cm2)	Voc(V)	FF	PCE(%)
Control	10.02±0.3	0.84±0.01	0.57±0.02	4.75±0.12
20 wt% PS	7.6±0.4	0.85±0.02	0.35±0.03	2.28±0.25

Table 2. 2 Parameters of BHJ devices based on PCDTBT:PCBM with and without 20%wt 650k PS

Examination of table 2.3 shows that the fill factor remains essentially constant with molecular weight, indicating that the addition of the third phase does not affect the recombination rate. On the other hand, the increase in total current, which seems to be responsible for the enhanced efficiency, indicates that the hole mobility may be one factor. In order to isolate the effect of the PS molecular weight on hole mobility hole-only diodes were fabricated with PEDOT:PSS and MoO_3 as the electron blocking layers. The measured J–V characteristics of the diodes were fitted with the Mott–Gurney equation[31]and the results are plotted as a function of MW, in figure 2.6a. From the figure we can see that the hole mobility increase with increasing PS molecular weight.

The functional form appears to be nearly the same as that of the efficiency, except that the absolute values of the mobility exceed those of the control for all molecular weights tested, achieving values of 1.75 x $10^{-4}cm^{-2}v^{-1}s^{-1}$ or nearly five times the control values before reaching the plateau values at Mw=2M-7M.

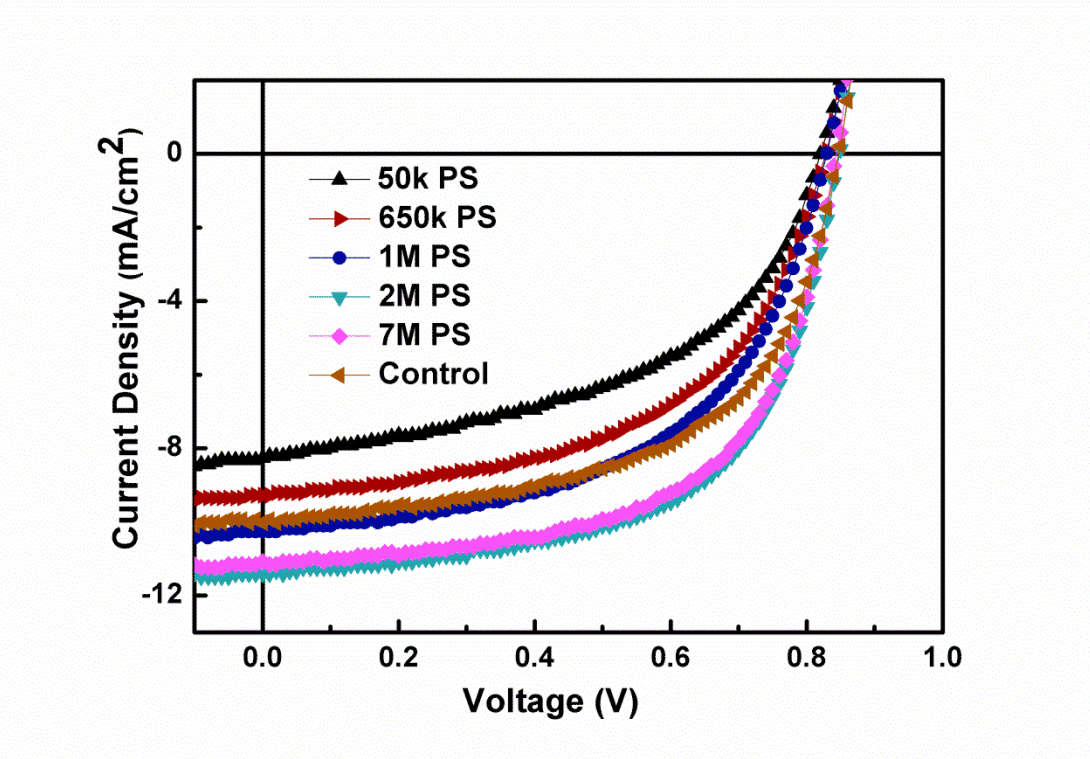

Figure 2. 4 Current density–voltage (J–V) characteristics of BHJ devices based on PCDTBT:PCBM with different MW PS

Material	Jsc(mA/cm2)	Voc(V)	FF	PCE(%)
PCDTBT:PCBM	10.02±0.3	0.84±0.01	0.57±0.02	4.75±0.12
50kPS:PCDTBT:PCBM	8.38±0.5	0.84±0.02	0.48±0.03	3.36±0.27
650kPS:PCDTBT:PCBM	9.50±0.4	0.82±0.02	0.52±0.03	3.99±0.24
1MPS:PCDTBT:PCBM	10.03±0.3	0.82±0.01	0.55±0.02	4.52±0.12
2MPS:PCDTBT:PCBM	11.25±0.4	0.85±0.01	0.60±0.02	5.74±0.15
7MPS:PCDTBT:PCBM	11.25±0.4	0.84±0.02	0.59±0.02	5.58±0.20

Table 2. 3 Device parameters of BHJ devices based on PCDTBT:PCBM with different MW PS

Milner[32]has shown that polymer crystalline nucleation dynamics are a function of the interfacial tension between the amorphous and crystalline phases of polyehtylene. In order to probe the relationship in our case which involves the dissimilar polymers, semi-crystalline PCDTBT and amorphous PS phases, we used nanoscale contact angle goniometry.The interfacial tension between two polymers can be determined using equation 1:

$$\gamma_{pcdtbt} = \gamma_{ps} \cos\theta + \gamma_{inter} \quad (1)$$

where γ_{pcdtbt} and $\gamma_{ps}$are the surface tensions of the two polymers ,$\gamma_{inter}$is the interfacial tension and θ is Young's contact angle.

The optimal annealing temperature for the PCDTBT device was reported be around 150 ^{o}C,[33]and hence, in order to apply equation 1 for measuring the interfacial tensions, we first determined the surface tensions of both PS and PCDTBT as a function of temperature. The surface tension measurements were conducted using the two-liquid (water and diiodomethane) contact angle method.[34]To obtain the temperature coefficient, we covered the sample stage with a hot plate and

checked the exact temperature of the polymer film surface using an infrared thermometer. The surface tension of PCDTBT and PS at different temperature points is shown in Figure 2.5, where we can see that the surface tensions of the two polymers are similar, where initially PS exhibited the higher values. With increased temperature the surface tension of PS falls more steeply that PCDTBT, such that above 150^{o}C, PS becomes the lower energy surface. Bilayer films were then formed, with PCDTBT, the polymer having the lower surface tension, spun cast onto the Si substrate and the polymer with the higher surface tension, PS, floated on top. The samples were then annealed at 150^{o}C for three days inorder to induce dewetting and achieve the equilibrium contact angle between phases. The contact angle between the droplets formed by the PS film and PCDTBT was directly measured using AFM and analyzed by the VEECO/DI contact angle software.[35]The contact angles are plotted in figure 2.6b as a function of molecular weight, where it can be seen that they increase with increasing molecular weight, reaching a plateau above Mw=2M.Substituting the values of the surface tension at 150 ^{o}C into equation 1 we can derive the interfacial tension between the polymers, which can then be substituted into equations 2 and 3 to obtain the chi parameter, χ, as well as the interfacial width,W, describing the degree of immiscibility. The results are shown in table 3.

$$\gamma = a\rho k_B T\sqrt{\frac{\chi}{6}} \quad (2)$$

$$W = \frac{2a}{\sqrt{6\chi}} \quad (3)$$

Where a is the effective length per monomer unit,ρ is the monomer density,k_B is the Boltzman constant and T is the termperature.

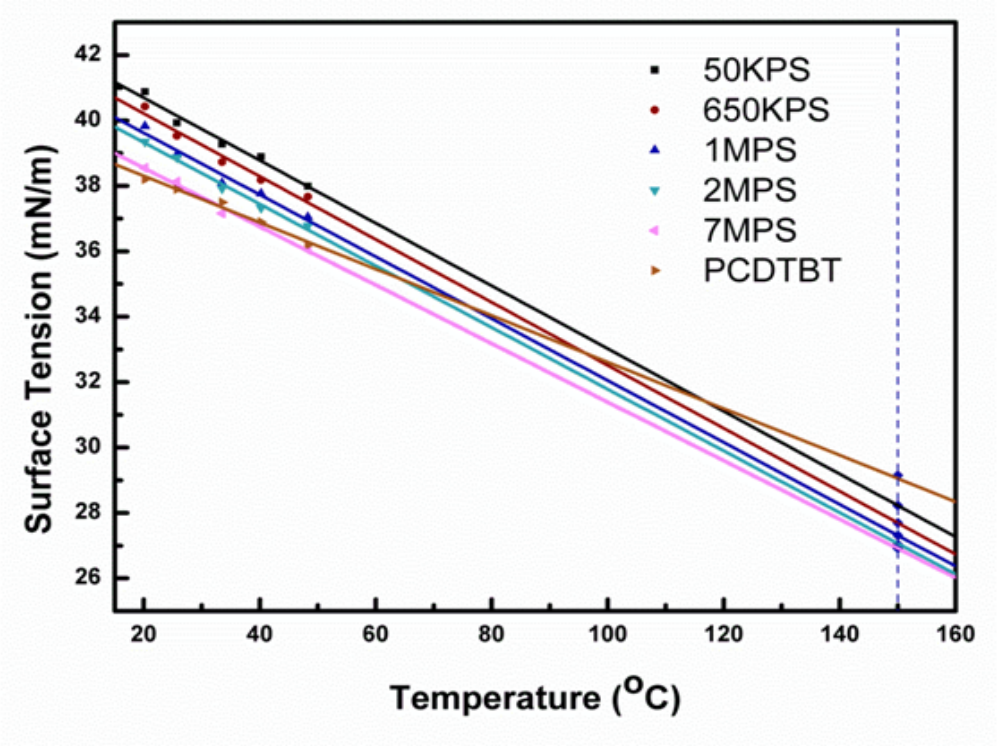

Figure 2. 5 Surface tension of PS and PCDTBT as a function of temperature

Polymer	Interfacial tension $\gamma_{PS/PCDTBT}$ (mN/m)	Huggins interaction parameter (χ)	Interfacial width W (Å)
50k PS	1.19 ± 0.04	0.086	18.66
650k PS	1.86 ± 0.03	0.212	11.88
1M PS	2.63 ± 0.06	0.423	8.41
2M PS	3.39 ± 0.08	0.703	6.52
7M PS	3.55 ± 0.08	0.772	6.22

Table 2. 4 The interaction parameters of PCDTBT and PS with different MW

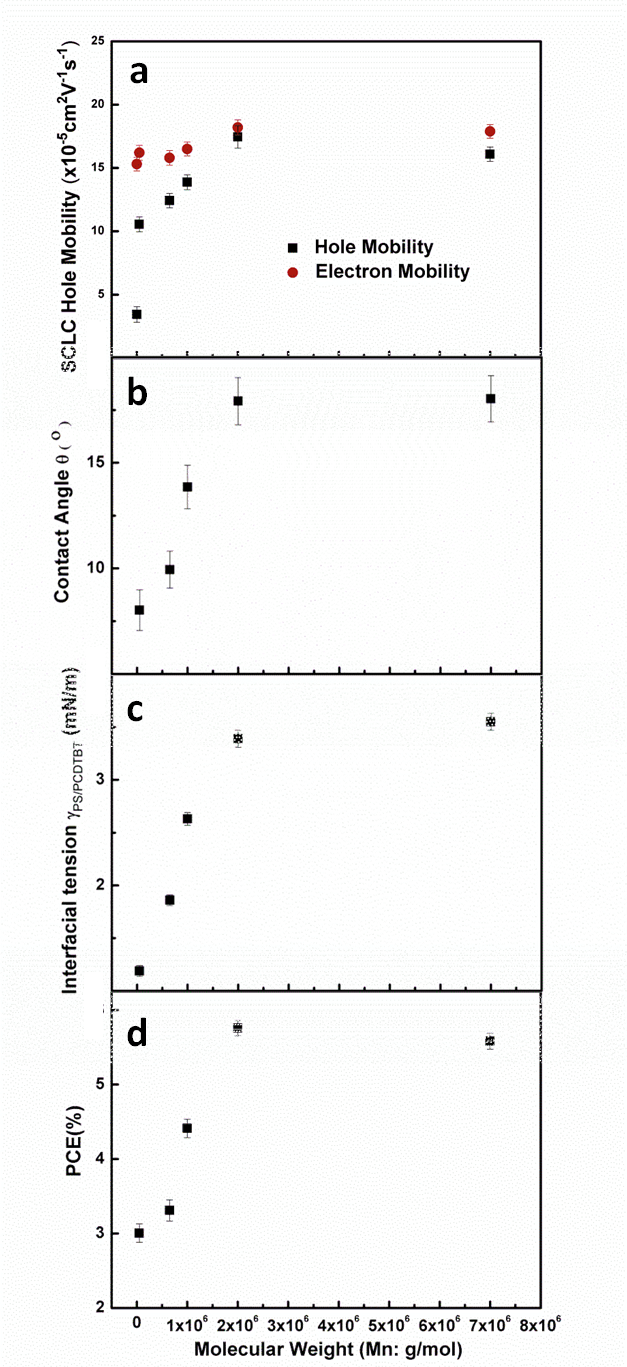

Figure 2. 6 BHJ Photovoltaic parameters of a PCDTBT/PCBM photovoltaic BHJ organic solar cell containing 2.5% PS, plotted as a function of the PS molecular weight; (a) Hole mobility of PCDTBT:PCBM with different MW PS (b) Contact angle between PCDTBT and PS with different MW (c) Interfacial tension between PCDTBT and PS with different MW (d) Device efficiency as a function of PS MW

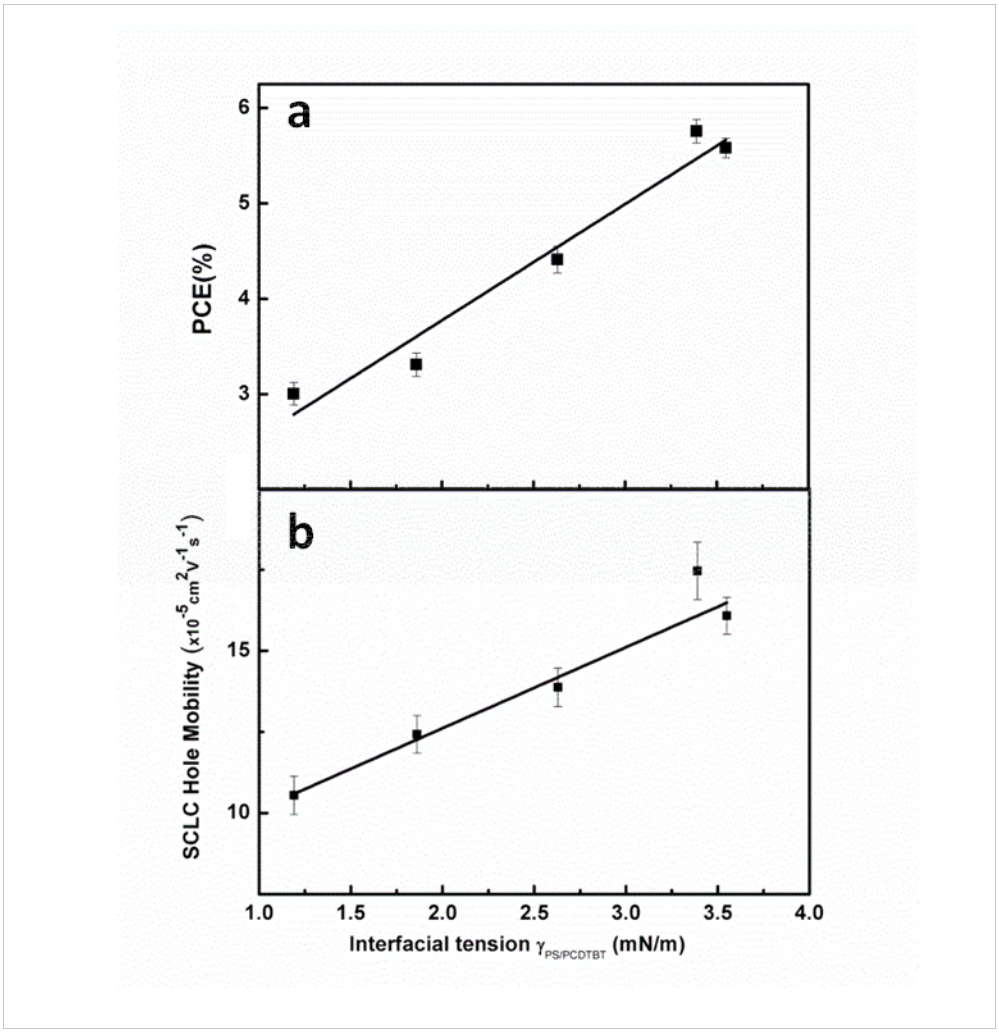

Figure 2. 7 (a) Hole mobility as a function of interfacial tension (b) Device efficiency as a function of interfacial tension

The interfacial tension is plotted as a function of molecular weight in figure 2.6c, where we can see that it also increases with molecular weight reaching a plateau in the region of Mw=2M-7M. Therefore comparing figures 2.6a-d, we find that they all have a similar functional form, where they increase linearly with molecular weight, reaching a plateau at Mw=2M. In figure 2.7 we plot the hole mobilityas a function of interfacial energy, consistent with the hypothesis that decreasing interfacial width enhances the crystalline nucleation and hence hole mobility. The electron mobility were also measured as a function of PS molecular weight and the results are shown with red dot in figure 2.6a, where we can see that there is nearly no difference between the samples with added PS and control sample, regardless of PS molecular weight.

2.3.2 Crystallinity and Vertical structure

Crystalline orientation and degree of crystallinity can further be measured using wide angle x-ray scattering (WAXS). Figure 2.8 shows the two-dimensional glancing incidence, GIWAXS, spectra obtained, at two glancing incidence angles, 0.12°and 0.14°, of the PCDTBT/PCBM blend films with 2.5% weight percent PS of different molecular weight. The spectra obtained above the critical angle, zeta= 0.12°, is sensitive to the structure of the film near surface, while the spectra obtained at the angle below the critical value probes the interior of the film. In all spectra distinct scattering rings are visible, having q -values of 0.33, 0.67, 1.36, and 2.0 A^{-1}. The broad, diffuse rings at 0.67, 1.36, and 2.0 $Å^{-1}$ correspond to the crystalline PCBM domains.[36, 37]The peaks at 0.33and 1.36$Å^{-1}$ are attributed to the distance between the PCDTBT backbones separated by the long alkyl side-chains in the edge on configuration and the distance between π - π stacked polymer backbones in the face on configuration, respectively.[20]However, it is not possible to assess if the scattering from the PCDTBT π - π stacking in these PCDTBT: PCBM blend films is most intense in the out-of-plane direction because this peak is also dominated by the PCBM ring in the scattering ring.[38]

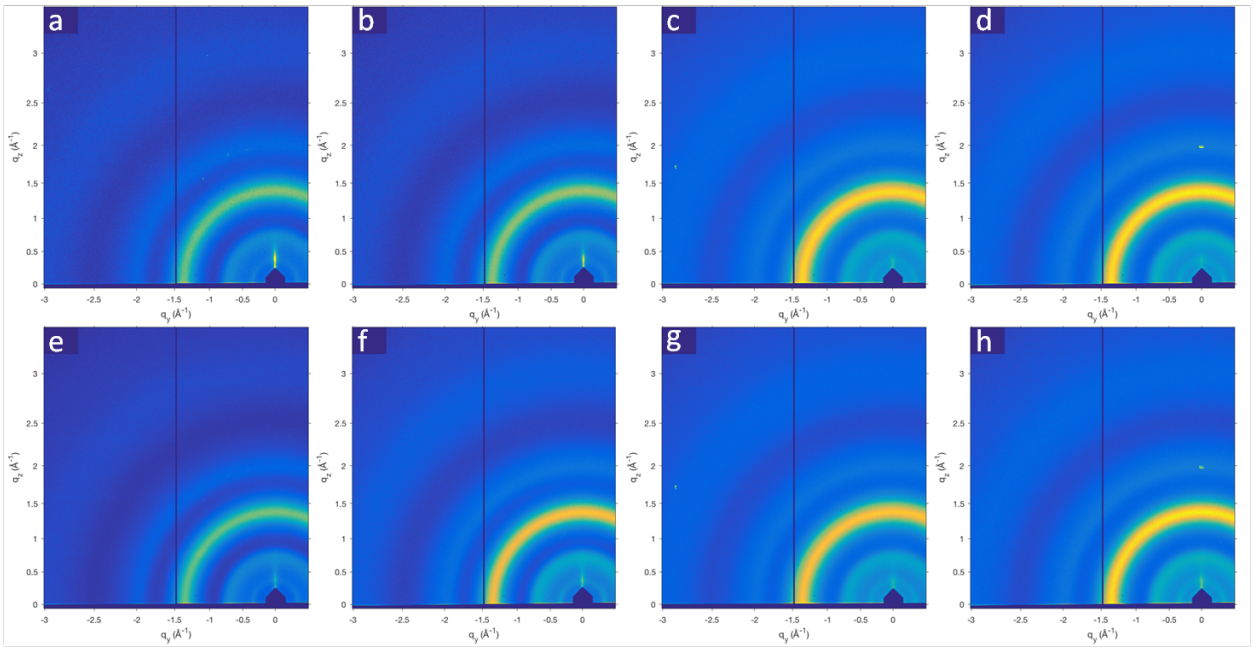

Figure 2. 8 GIWAXS data of PCDTBT:PCBM blends film with surface mode: (a) control (b) 50k PS (c) 1M PS (d) 2M PS; and film mode: (e) control (f) 50k PS (g) 1M PS (h) 2M PS

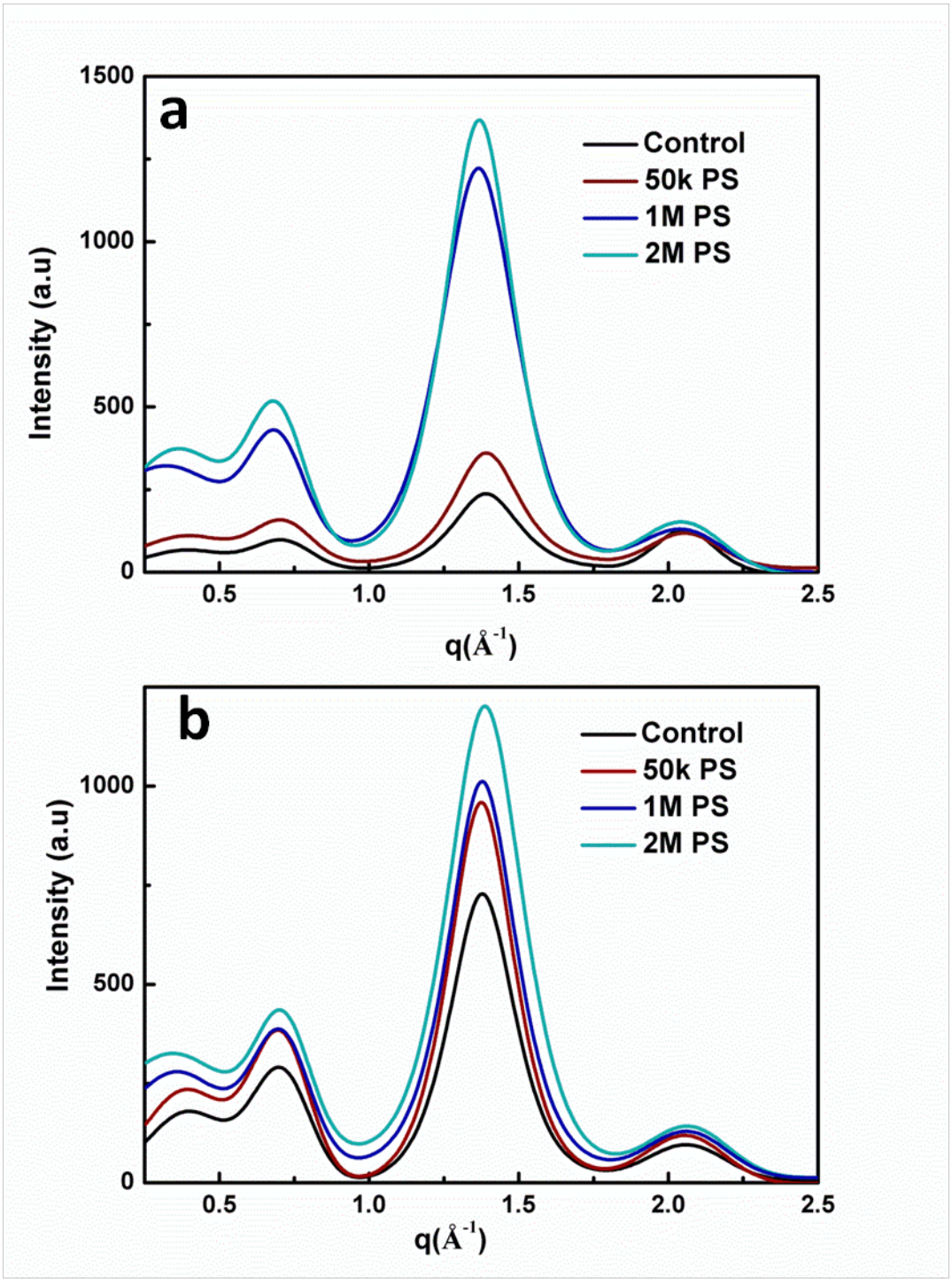

Figure 2. 9 GIWAXS profiles of PCDTBT:PCBM blend films with different molecular weight of PS: (a) surface mode (b) film mode

Figure 2.9 shows the one-dimensional GIWAXS profiles of PCDTBT:PCBM blends film with different molecular weight of PS under surface mode and film mode. In surface mode, it is clear that the multiple peak intensities with high molecular weight PS are much higher than those with low molecular weight PS and without PS, indicating an increase in crystallinity of PCDTBT and PCBM. In film mode, the multiple peak intensities with low molecular weight PS are also enhanced compared with the control, suggesting addition of low molecular weight PS (50k) mainly influenced the region in the film outside of the topmost surface.

The efficiency of the holes in reaching the electrode is another important factor determining the overall efficiency of a BHJ solar cell. In this case, since we are using an inverted configuration for the BHJ cell, the nature of the free air surface is critical for establishing a good connection with the hole acceptor electrode. From table 2.4 we find that the surface tension of PS at 150^{o}C nearly the same as that of PCDTBT at that temperature, and independent of polymer molecular weight. Therefore in a binary blend of the two polymers, surface segregation would be driven primarily by minimizing the interfacial tension between the two polymers. The interfacial tension between the two polymers is strongly dependent on the PS molecular weight where we can see from table2.4 that the Flory Chi parameter differs by nearly an order of magnitude. Hence the driving force for surface segregation is also expected to be a strong function of the polymer molecular weight.

In order to determine the structure of the air interface, TOF-SIMS was employed to obtain the film composition as a function of depth. Deuterated PS (d-PS) was used as the additive because of the excellent sensitivity of TOF-SIMS for detecting ^{2}H. Figure 2.10 shows the SIMS profiles for the dPS volume fraction in PCDTBT:PCBM blends film with dPS of different molecular weights. From Figure 2.10, we find that 50k PS tends to aggregated at the substrate. When 1M dPS was introduced in the film, 1M dPS aggregated at the surface and the substrate. With the molecular weight of dPS increased to 2M, dPS is distributed mostly at the surface in the blendfilm.

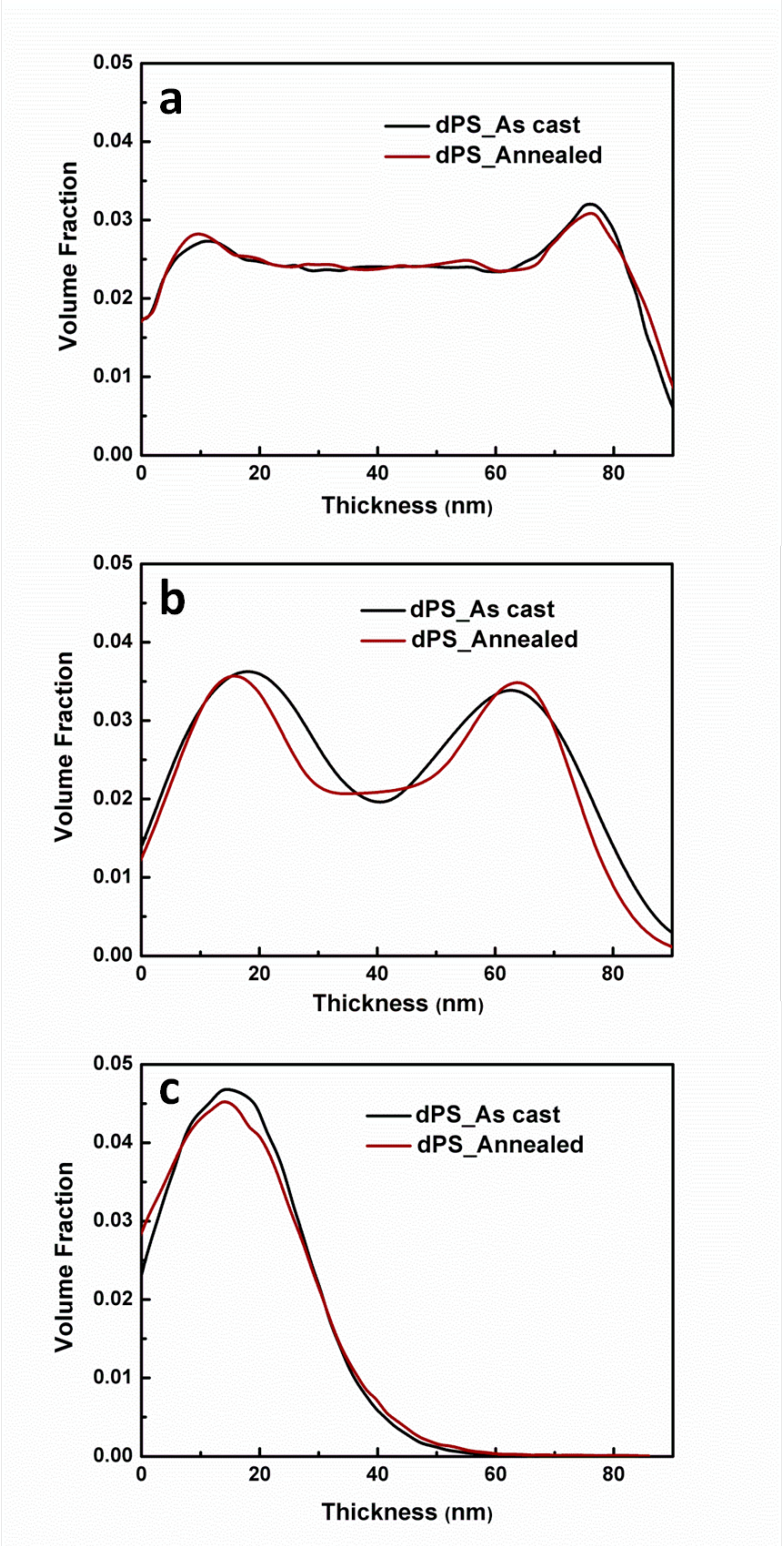

Figure 2. 10 SIMS depth profiles for dPS volume fraction in different PCDTBT:PCBM blends film (a) 50k PS ; (b) 1M PS ; (c) 2M PS.

Figure 2.11 shows the SIMS profiles for the PCBM volume fraction in PCDTBT:PCBM blends film with different PS. From Figure 2.11, one finds that PCBM aggregated at the surface in the film of control sample and annealing promoted this aggregation. With 50k PS, the aggregation of PCBM at the surface is maintained in the blend film. When 1M PS was introduced in the film, the aggregation of PCBM at surface is mitigated. With the molecular weight of PS increased to 2M, the distribution of PCBM at the surface is greatly reduced compared to the control since 2M PS is distributed mostly at the surface in the blend film. The migration of PS to the surface mitigated the aggregation of PCBM in the active layer and thus optimized vertical morphology, which would lead to higher efficiency. The migration of PS to the surface with increased molecular weight is consistent with X-ray data, which suggests low molecular weight PS (50k) mainly influenced the region in the film outside of the topmost surface and high molecular PS mainly influenced the topmost surface.

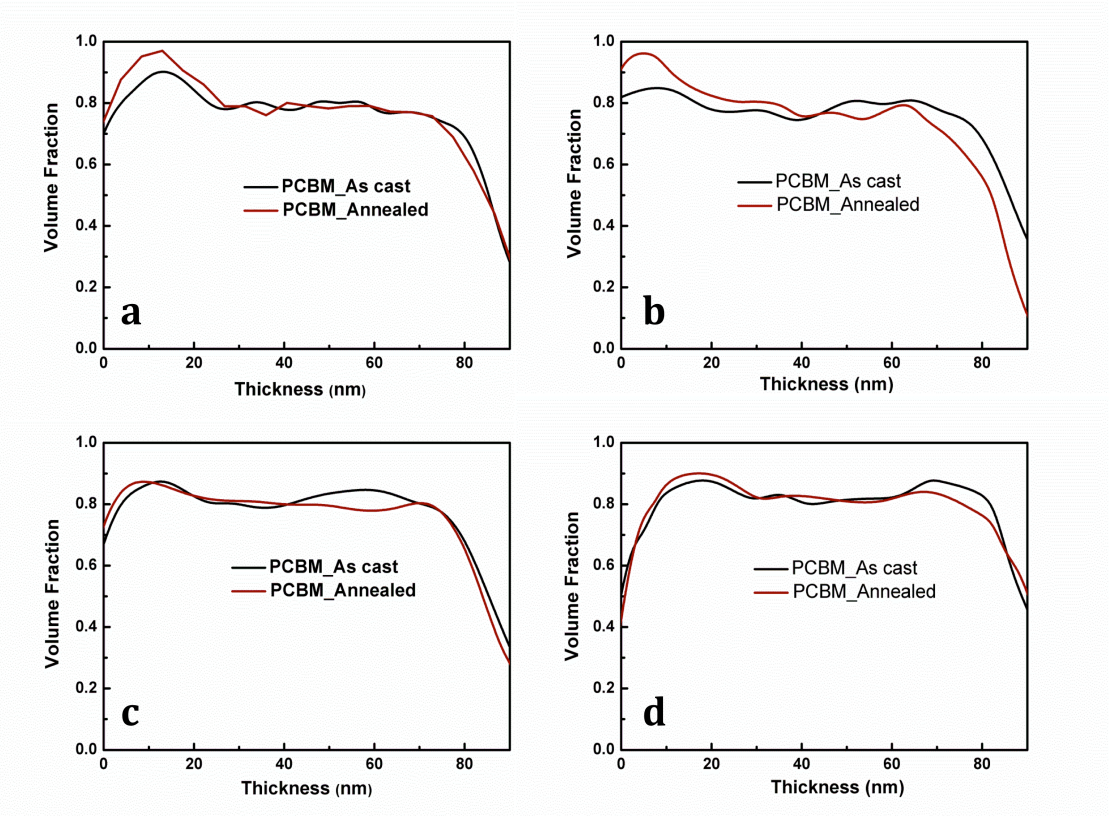

Figure 2. 11 SIMS profiles for the PCBM volume fraction in different PCDTBT:PCBM blends film: (a) control ; (b) 50k PS ; (c) 1M PS ; (d) 2M PS.

2.3.3 Morphology of Blend Sample

In figure 2.12we show AFM topography and friction scans of the surfaces, together with TEM images. From the figures we can see that for low Mw samples, both AFM and TEM images show a uniform surface composition. For the high molecular weight samples, topographical images indicate small depressions on the surface, which the friction scans show to be a component with lower friction coefficients. TEM scans show white regions of the same diameter, identifying these regions as the PS phase. Hence the large surface segregated structures shown in the SIMS figures are not laterally homogenous, explaining the broad structures observed. A cartoon representation of the chemical structure at the surface of these films is shown in figure 2.13. PCBM is has a lower surface tension than the polymers and segregates easily to free air interface. Since PCBM is the electron acceptor in this structure, it forms an electronic block to the conduction of holes to the electrodes in the inverted structure. In figure 2.13b we show a schematic of the surface when low molecular weight PS is mixed with PCDTBT/PCBM. In this case the interfaces are broad, the domains are small, and only a small fraction participates in nucleation of the crystalline domains. Furthermore, the PS domains do not segregate to the free air surface, leaving the PCBM layer intact. The addition of non-photoactive polymer as well as the disruption of the PCBM phase segregated domains within the material decrease the overall efficiency. In figure 2.13c we show the structure when high Mw PS is added. In this case the high interfacial energy drives the PS domains to the free surface, reducing the overall contact areas with the PCDTBT polymer matrix. The PS domains displace and disrupt the PCBM layer, increasing access for the hole current to the electrodes. Furthermore, the enhanced nucleation of the face-on configuration further enhances the current, contributing the high hole mobility being measured.

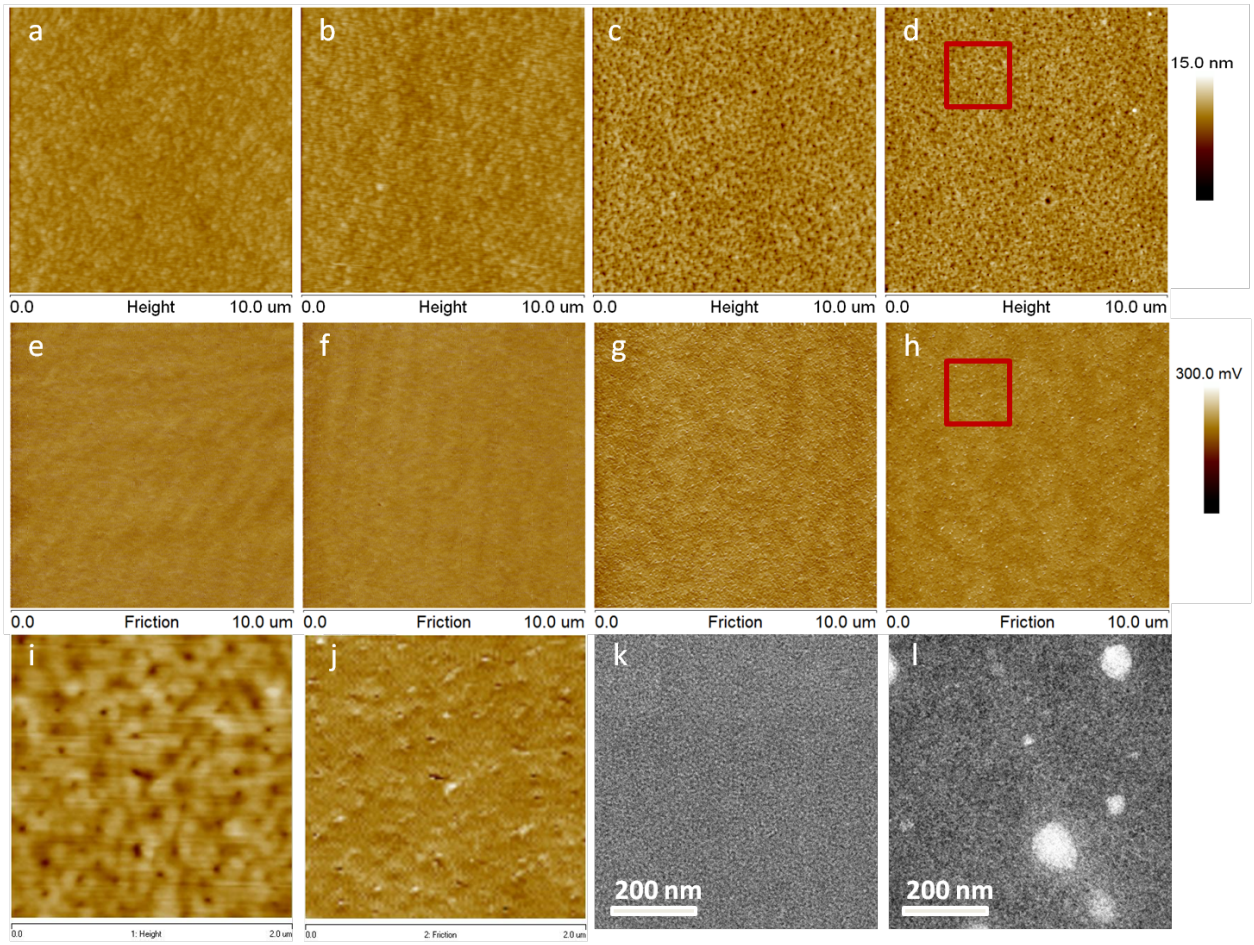

Figure 2. 12 AFM topography images for different PCDTBT:PCBM blend films:(a) control (b) 50KPS (d) 1M PS (d) 2M PS. (e) , (f) ,(g) and (h) are corresponding lateral force images for samples shown in (a), (b) ,(c) and (d). (i) and (j) are corresponding magnified images for the region delineated by red squares in (d) and (h). TEM images for PCDTBT:PCBM blend films (k) control (l) 2M PS.

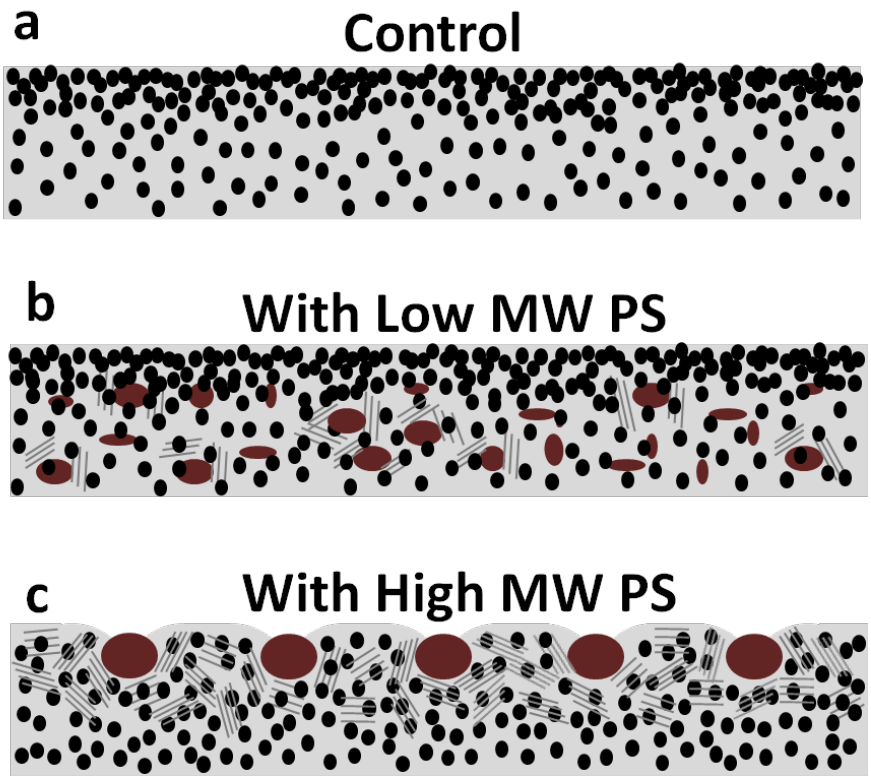

Figure 2. 13 Schematic representation of the chemical structure at the surface of PCDTBT/PCBM films with different MW PS. The black dot represents PCBM, red dot represents PS and grey rod represents crystalline of PCDTBT.

2.4 Conclusion

In conclusion we have shown that the addition of a low volume fraction of high molecular weight PS to PCDTBT:PCBM polymer blend can enhance the overall efficiency of BHJ photovoltaic cells. The enhancement increases with molecular weight reaching a plateau above Mw=2M. This phenomena is explained in terms of increasing interfacial tension, which in turn drives the PS to the film surface, disrupting the PCBM layer, and enhancing the collection efficiency of the hole charge carriers.

Reference

1. Van Franeker, J. J.; Turbiez, M.; Li, W. W.; Wienk, M. M.; Janssen, R. A. J. A real-time study of the benefits of co-solvents in polymer solar cell processing. *Nat Commun* 2015, 6.

2. Krebs, F. C. All solution roll-to-roll processed polymer solar cells free from indium-tin-oxide and vacuum coating steps. *Org. Electron.* 2009, 10, 761-768.

3. Voigt, M. M.; Mackenzie, R. C. I.; Yau, C. P.; Atienzar, P.; Dane, J.; Keivanidis, P. E.; Bradley, D. D. C.; Nelson, J. Gravure printing for three subsequent solar cell layers of inverted structures on flexible substrates. *Sol. Energy Mater. Sol. Cells* 2011, 95, 731-734.

4. Brabec, C. J.; Sariciftci, N. S.; Hummelen, J. C. Plastic solar cells. *Adv. Funct. Mater.* 2001, 11, 15-26.

5. Waldauf, C.; Morana, M.; Denk, P.; Schilinsky, P.; Coakley, K.; Choulis, S. A.; Brabec, C. J. Highly efficient inverted organic photovoltaics using solution based titanium oxide as electron selective contact. *Appl. Phys. Lett.* 2006, 89.

6. Hau, S. K.; Yip, H.-L.; Jen, A. K. Y. A Review on the Development of the Inverted Polymer Solar Cell Architecture. *Polymer Reviews* 2010, 50, 474-510.

7. Li, G.; Chu, C. W.; Shrotriya, V.; Huang, J.; Yang, Y. Efficient inverted polymer solar cells. *Appl. Phys. Lett.* 2006, 88.

8. Ameri, T.; Dennler, G.; Waldauf, C.; Azimi, H.; Seemann, A.; Forberich, K.; Hauch, J.; Scharber, M.; Hingerl, K.; Brabec, C. J. Fabrication, Optical Modeling, and Color Characterization of Semitransparent Bulk-Heterojunction Organic Solar Cells in an Inverted Structure. *Adv. Funct. Mater.* 2010, 20, 1592-1598.

9. Yang, T.; Cai, W.; Qin, D.; Wang, E.; Lan, L.; Gong, X.; Peng, J.; Cao, Y. Solution-Processed Zinc Oxide Thin Film as a Buffer Layer for Polymer Solar Cells with an Inverted Device Structure. *J. Phys. Chem. C* 2010, 114, 6849-6853.

10. Sun, Y.; Seo, J. H.; Takacs, C. J.; Seifter, J.; Heeger, A. J. Inverted Polymer Solar Cells Integrated with a Low-Temperature-Annealed Sol-Gel-Derived ZnO Film as an Electron Transport Layer. *Adv. Mater.* 2011, 23, 1679-1683.

11. Hsieh, C.-H.; Cheng, Y.-J.; Li, P.-J.; Chen, C.-H.; Dubosc, M.; Liang, R.-M.; Hsu, C.-S. Highly Efficient and Stable Inverted Polymer Solar Cells Integrated with a Cross-Linked Fullerene Material as an Interlayer. *J. Am. Chem. Soc.* 2010, 132, 4887-4893.

12. Park, J. S.; Lee, B. R.; Lee, J. M.; Kim, J. S.; Kim, S. O.; Song, M. H. Efficient hybrid organic-inorganic light emitting diodes with self-assembled dipole molecule deposited metal oxides. *Appl. Phys. Lett.* 2010, 96.

13. Pan, C.; Li, H.; Akgun, B.; Satijia, S. K.; Zhu, Y.; Xu, D.; Ortiz, J.; Gersappe, D.; Rafailovich, M. H. Enhancing the Efficiency of Bulk Heterojunction Solar Cells via Templated Self-Assembly. *Macromolecules* 2013, 46, 1812-1819.

14. Bedford, N. M.; Dickerson, M. B.; Drummy, L. F.; Koerner, H.; Singh, K. M.; Vasudev, M. C.; Durstock, M. F.; Naik, R. R.; Steckl, A. J. Nanofiber-Based Bulk-Heterojunction Organic Solar Cells Using Coaxial Electrospinning. *Adv. Energy. Mater.* 2012, 2, 1136-1144.

15. Scharber, M. C.; Sariciftci, N. S. Efficiency of bulk-heterojunction organic solar cells. *Prog. Polym. Sci.* 2013, 38, 1929-1940.

16. Liu, F.; Gu, Y.; Shen, X.; Ferdous, S.; Wang, H.-W.; Russell, T. P. Characterization of the morphology of solution-processed bulk heterojunction organic photovoltaics. *Prog. Polym. Sci.* 2013, 38, 1990-2052.

17. Chen, L.-M.; Hong, Z.; Li, G.; Yang, Y. Recent Progress in Polymer Solar Cells: Manipulation of Polymer:Fullerene Morphology and the Formation of Efficient Inverted Polymer Solar Cells. *Adv. Mater.* 2009, 21, 1434-1449.

18. Collins, B. A.; Gann, E.; Guignard, L.; He, X.; McNeill, C. R.; Ade, H. Molecular Miscibility of Polymer−Fullerene Blends. *The Journal of Physical Chemistry Letters* 2010, 1, 3160-3166.

19. Kim, M.; Lee, J.; Jo, S. B.; Sin, D. H.; Ko, H.; Lee, H.; Lee, S. G.; Cho, K. Critical factors governing vertical phase separation in polymer-PCBM blend films for organic solar cells. *J Mater Chem A* 2016, 4, 15522-15535.

20. Tremolet de Villers, B. J.; MacKenzie, R. C. I.; Jasieniak, J. J.; Treat, N. D.; Chabinyc, M. L. Linking Vertical Bulk-Heterojunction Composition and Transient Photocurrent Dynamics in Organic Solar Cells with Solution-Processed MoOx Contact Layers. *Adv. Energy. Mater.* 2014, 4, n/a-n/a.

21. Huang, J.; Carpenter, J. H.; Li, C.-Z.; Yu, J.-S.; Ade, H.; Jen, A. K. Y. Highly Efficient Organic Solar Cells with Improved Vertical Donor–Acceptor Compositional Gradient Via an Inverted Off-Center Spinning Method. *Adv. Mater.* 2016, 28, 967-974.

22. Xiao, Z.; Yuan, Y.; Yang, B.; VanDerslice, J.; Chen, J.; Dyck, O.; Duscher, G.; Huang, J. Universal Formation of Compositionally Graded Bulk Heterojunction for Efficiency Enhancement in Organic Photovoltaics. *Adv. Mater.* 2014, 26, 3068-3075.

23. Wang, H.; Gomez, E. D.; Kim, J.; Guan, Z.; Jaye, C.; Fischer, D. A.; Kahn, A.; Loo, Y.-L. Device Characteristics of Bulk-Heterojunction Polymer Solar Cells are Independent of Interfacial Segregation of Active Layers. *Chem. Mater.* 2011, 23, 2020-2023.

24. Li, H.; Yang, Z.; Pan, C.; Jiang, N.; Satija, S.; Xu, D.; Gersappe, D.; Nam, C.-Y.; Rafailovich, M. H. A new strategy to engineer polymer bulk heterojunction solar cells with thick active layers via self-assembly of tertiary columnar phase. *Nanoscale* 2017.

25. Sun, Z.; Xiao, K.; Keum, J. K.; Yu, X.; Hong, K.; Browning, J.; Ivanov, I. N.; Chen, J.; Alonzo, J.; Li, D.; Sumpter, B. G.; Payzant, E. A.; Rouleau, C. M.; Geohegan, D. B. PS-b-P3HT Copolymers as P3HT/PCBM Interfacial Compatibilizers for High Efficiency Photovoltaics. *Adv. Mater.* 2011, 23, 5529-5535.

26. Huh, Y. H.; Park, B. Interface-engineering additives of poly(oxyethylene tridecyl ether) for low-band gap polymer solar cells consisting of PCDTBT:PCBM70 bulk-heterojunction layers. *Opt. Express* 2013, 21, A146-A156.

27. Chu, T. Y.; Alem, S.; Verly, P. G.; Wakim, S.; Lu, J. P.; Tao, Y.; Beaupre, S.; Leclerc, M.; Belanger, F.; Desilets, D.; Rodman, S.; Waller, D.; Gaudiana, R. Highly efficient polycarbazole-based organic photovoltaic devices. *Appl. Phys. Lett.* 2009, 95.

28. Anastasiadis, S. H.; Gancarz, I.; Koberstein, J. T. Interfacial tension of immiscible polymer blends: temperature and molecular weight dependence. *Macromolecules* 1988, 21, 2980-2987.

29. Xue, H. L.; Kong, X. Z.; Liu, Z. R.; Liu, C. X.; Zhou, J. R.; Chen, W. Y.; Ruan, S. P.; Xu, Q. TiO2 based metal-semiconductor-metal ultraviolet photodetectors. *Appl. Phys. Lett.* 2007, 90.

30. Vohra, V.; Campoy-Quiles, M.; Garriga, M.; Murata, H. Organic solar cells based on nanoporous P3HT obtained from self-assembled P3HT:PS templates. *J. Mater. Chem.* 2012, 22, 20017-20025.

31. Huang, Y.; Wen, W.; Mukherjee, S.; Ade, H.; Kramer, E. J.; Bazan, G. C. High-Molecular-Weight Insulating Polymers Can Improve the Performance of Molecular Solar Cells. *Adv. Mater.* 2014, 26, 4168-4172.

32. Milner, S. T. Polymer crystal-melt interfaces and nucleation in polyethylene. *Soft Matter* 2011, 7, 2909-2917.

33. Wong, H. C.; Li, Z.; Tan, C. H.; Zhong, H.; Huang, Z.; Bronstein, H.; McCulloch, I.; Cabral, J. T.; Durrant, J. R. Morphological Stability and Performance of Polymer–Fullerene Solar Cells under Thermal Stress: The Impact of Photoinduced PC60BM Oligomerization. *ACS Nano* 2014, 8, 1297-1308.

34. Guo, Y.; He, S.; Yang, K.; Xue, Y.; Zuo, X.; Yu, Y.; Liu, Y.; Chang, C.-C.; Rafailovich, M. H. Enhancing the Mechanical Properties of Biodegradable Polymer Blends Using Tubular Nanoparticle Stitching of the Interfaces. *ACS Appl. Mater. Interfaces* 2016, 8, 17565-17573.

35. Pack, S.; Kashiwagi, T.; Cao, C.; Korach, C. S.; Lewin, M.; Rafailovich, M. H. Role of Surface Interactions in the Synergizing Polymer/Clay Flame Retardant Properties. *Macromolecules* 2010, 43, 5338-5351.

36. Yin, W.; Dadmun, M. A New Model for the Morphology of P3HT/PCBM Organic Photovoltaics from Small-Angle Neutron Scattering: Rivers and Streams. *ACS Nano* 2011, 5, 4756-4768.

37. Pearson, A. J.; Wang, T.; Dunbar, A. D. F.; Yi, H.; Watters, D. C.; Coles, D. M.; Staniec, P. A.; Iraqi, A.; Jones, R. A. L.; Lidzey, D. G. Morphology Development in Amorphous Polymer:Fullerene Photovoltaic Blend Films During Solution Casting. *Adv. Funct. Mater.* 2014, 24, 659-667.

38. Lu, X. H.; Hlaing, H.; Germack, D. S.; Peet, J.; Jo, W. H.; Andrienko, D.; Kremer, K.; Ocko, B. M. Bilayer order in a polycarbazole-conjugated polymer. *Nat Commun* 2012, 3.

Chapter 3. The Effect of Graphene and Graphene Oxide on the Interdiffusion of PMMA Thin Film

3.1 Introduction

Graphene and graphene derivatives such as graphene oxide (GO) have received increasing interest due to their unique two-dimensional structure and outstanding mechanical, thermal, and electrical properties as well as large surface area.[1-5]Based on those excellent properties, graphene and GO have been regarded as ideal functional nanofillers for improving mechanical, electrical, thermal, and gas barrier performance of polymers.[6-9] The polymer/graphene and polymer/GO nanocomposite have shown promising potential for a wide range of applications such as supercapacitor, reinforced materials, fuel cell and solar cell.[10-15]Although considerable research has been devoted to investigating the enhanced properties and compatibilization effect of graphene and GO in bulk polymer-blend nanocomposites,[16, 17]little attention has been paid to the dynamics and morphology of graphene and GO doped polymer thin films.

Polymer thin films are proving to be increasingly important because of their indispensable role in applications such as protective coatings, lubricants, decorative paints, adhesives, biomembranes, sensors, as active layers in devices such as organic light-emitting diodes (OLED), organic field effect transistors (OFET), organic solar cells and organic laser devices, and to modify surface wettabilities.[18-24] The confinement of polymers in thin films influences the dynamic properties and wetting characteristics, hence polymer thin films exhibit different physical properties compared with bulk polymers.[25] Multilayer polymer thin films in particular have numerous practical applications because of their potential for combining different homopolymer attributes.[26-29] However, a persistent concern with multilayer polymer thin films is their stability against dewetting, which is caused by the unfavorable interfacial tension between most polymers.[30] Kim have shown that the dewetting behavior of PMMA/PS bilayer films is significantly inhibited by GO monolayers at the polymer-polymer interface due to the favorable interaction of GO with both PS and PMMA[31]. Here, we show that the dewetting can also be

controlled by adding graphene and GO into polymer thin films instead of depositing monolayer at the interface.

In this work, we investigated the influence of graphene and GO loading on the dewetting behavior of polymer thin films and correlate the data with interdiffusion measurements. The interdiffusion rate of polymer thin films is inhabited by GO while graphene does not affect the diffusion of polymer chains. The results show that GO are more effective at stabilizing the films due the more favorable interaction of GO with the polymer thin film.

3.2 Experiment

3.2.1 Materials

Poly(methyl methacrylate) (PMMA) with molecular weight of 106K and PS (MW=2000K) are purchased from Polymer Sources Inc. Dimethylformamide (DMF) is purchased from Sigma-Aldrich Co. LLC. Graphene and GO were from Graphene Laboratories Inc.

3.2.2 PMMA Bilayer Sample Preparation

Si(100) wafers were partitioned to 2x2 cm^2 and then treated with a modified Shiraki technique: the substrates were immersed in H_2O:H_2O_2:H_2SO_4 (3: 1:1 vol) solution for 15 min at 80 °C, rinsed in deionized water, and immersed in very diluted hydrofluoric acid solution H_2O:HF (15:1 vol) for 20 s at room temperature to create a hydrophobic surface.PMMA was chosen as the bottom layer for test purpose. The sample geometry is illustrated in Figure 3.1 PMMA (Mw=106K, Mw/Mn=1.05) and graphene or GO were dispersed in the toluene, in ratios ranging from 0.02% to 0.08% by weight. The resultant solutions were clear and stable for at least 3 weeks, indicating that the graphene and GO were well dispersed in the PMMA solution during the time of the experiment. The PMMA solution with graphene or GO was spun-cast onto HF etched Si wafers at 2000 rpm for 60s. The samples were then annealed at 150 °C in a vacuum of

10^{-3} Torr for 5 h to remove the residual solvent and relax strains induced by the spinning process. The thickness of the layers, 1200 ± 55 Å, was measured using ellipsometry. PS (Mw=2000K, Mw/Mn=1.06) dissolved in toluene was spun-cast onto Si substrate and then PS film with thickness of 300 ± 15 Å was carefully floated from DI water onto the PMMA layer on Si substrate. Control samples were prepared using the same procedure without graphene or graphene oxide. After preparation, the films were allowed to dry at room temperature for at least 12 h before annealing.

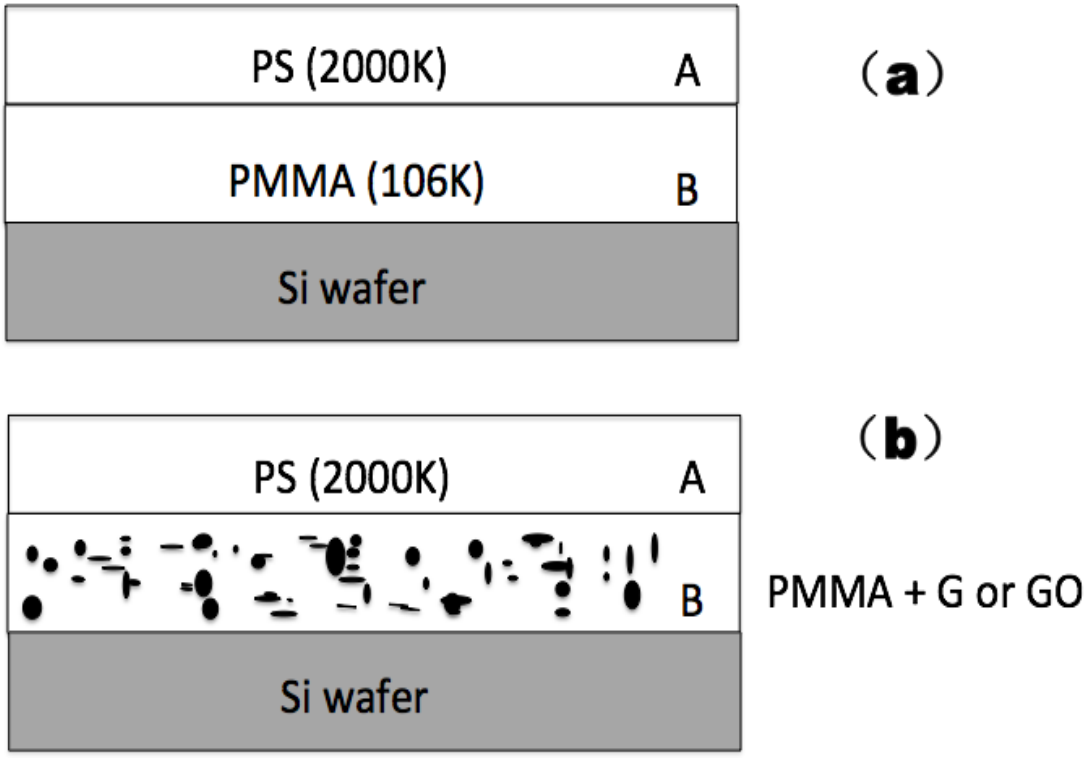

Figure 3. 1 Schematic of the sample geometry for the dewetting experiments. (a) A liquid PMMA layer, B, is spun-cast onto the substrate. A more viscous PS layer, A, is floated on top of the bottom layer. (b) To investigate the effect of graphene or GO on dewetting dynamics, the bottom PMMA layer is filled with graphene or GO.

3.2.3 Characterization Methods

Dewetting Measurement: To initiate dewetting, the PS/PMMA bilayer samples were annealed at a fixed temperature of 190 °C in a high-vacuum oven with a vacuum of 10^{-7} Torr for different annealing time. The samples were then quenched to room temperature and the diameters of the dewetting holes were measured by using an atomic force microscope (AFM) (Digital Instruments, USA) with a silicon nitride tip.

Neutron Reflectivity: The specular neutron reflectivity (NR) experiments were conducted with a NG7 reflectometer at the National Institute of Standards and Technology (Gaithersburg, MD, USA). The wavelength (λ_N) of the neutron beam was 0.47 nm, with $\Delta\lambda_N/\lambda_N$ = 2.5%. A wave vector magnitude, q_z, range 0.008−0.12 was scanned for the bilayer samples on silicon substrate, where $q_z = 4\pi\sin(\theta)/\lambda$ and θ is the angle of incidence. The data were reduced for varying incident beam intensity and background scattering and then fit by Reflpak software (NIST CNR).To obtain a good contrast between the polymer-polymer interface, deuterated poly(methyl methacrylate) (dPMMA) was used in neutron reflectivity experiment. The control bilayer samples were prepared by floating PMMA layer onto the dPMMA layer that was spun-cast on the HF etched thick silicon wafer in advance. For experimental samples, the graphene and GO nanoparticles were added into PMMA layer or dPMMA layer with the ratio of 0.1wt%and 0.02wt%respectively. Each sample was dried in a vacuum oven at 50 °C to remove residual water and then annealed at 150 °C with different annealing time.

Contact Angle measurement: The contact angle measurement was conducted to characterize the interaction between PMMA with the graphene and GO. The layers of graphene and GO were prepared by drop-casting the graphene and GO DMF dispersion on the Si wafers. The wafers with graphene and GO layers were imaged by SEM. PMMA pellets were cut into small pieces (around 5 mg) and located on the Si wafers covered with graphene and GO nanoparticles. To melt the polymer pieces and let them form droplets on the nanoparticle layers, the samples were put in a vacuum oven with the temperature at 180 °C, and then annealed for overnight. A CAM 200 optical contact angle meter (KSV Instrument Ltd., Helsinki, Finland) was used to measure the contact angles of PMMA droplets on each nanoparticle layer. The contact angle value represents the average measurements of 5 polymer droplets.

3.3 Results and Discussion

3.3.1 Dewetting Dynamics

In order to investigate the influence of grpahene and GO on the dewetting dynamics of polymer films, bilayer samples were prepared with graphene or GO doped PMMA film as bottom layer and PS film as top layer. The sample geometry is shown in Figure 3.1. The samples were annealed for different time to allow dewetting to occur. The dewetting hole growth of those samples were then studied using AFM. In the first row of Figure 3.2, we show topographical AFM images of the samples annealed for 12 h. The dewetting holes produced in the PS films floated on the PMMA substrates were clearly observed. Holes with smaller size (1.65 ± 0.15 μm) were seen in the sample with 0.04wt%graphene. For sample with 0.04wt% GO, the holes size is so small (0.65 ± 0.12 μm) that they can only be observed with a high magnification mode (40 μm scan size). After annealing for 24h, a significant increase is seen in the holes size (2.41± 0.27 μm to 3.96 ± 0.35 μm) and overlapping rims were also observed in the control sample, as shown in Figure 3.2d. In the case of the sample with 0.04 wt%graphene, the holes gradually grow and maintain their original round shape after annealing 24 h (Figure 3.2e).In the sample with 0.04wt%GO, however, the holes size does not increase much after annealing for additional 12 h at 190 °C. And the average size of holes only reaches 3.17 ± 0.36 μm even after annealing for 87 h(Figure 3.2g). This implies that the addition of GO into PMMA film is more effective than graphene at stabilization of bilayer thin films of PS/PMMA against dewetting.

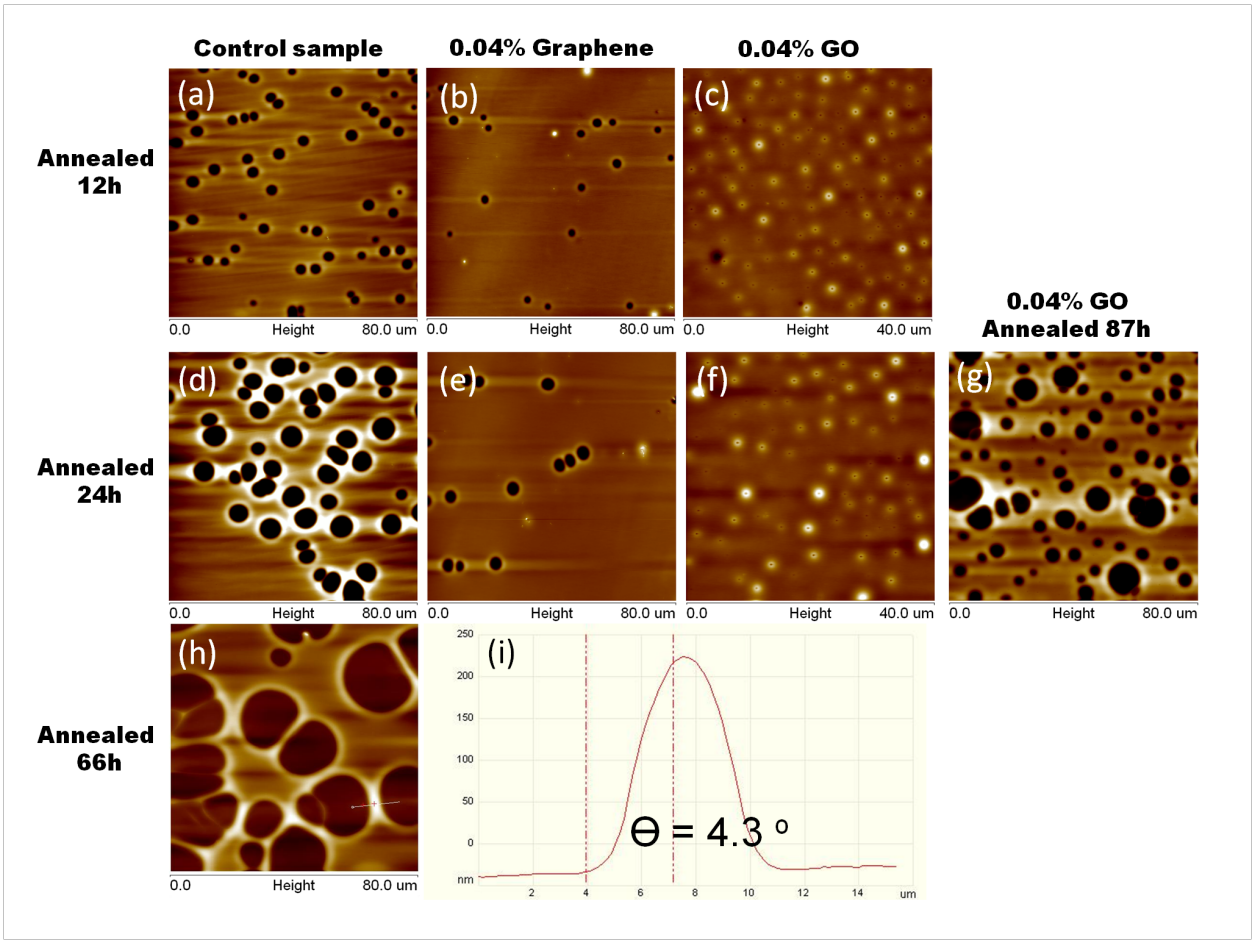

Figure 3. 2 AFM images of dewetting holes of PS films on the PMMA substrates unfilled and filled with 0.04% wt graphene and 0.04% wt GO annealed at 190 °C for (a-c) 12 h, (d-f) 24 h, (g) 87 h, and (h) 66 h. (i) Cross sectional scan and contact angle measurement corresponding to sample in (h).

According to the model developed by Brochard-Wyart et al,[30] the dewetting velocity (V) of the polymer layer is related to the relative viscosities of the PS and PMMA layers (n_{ps}, n_{pmma}), the surface and interfacial tension (r_{ps}, r_{pmma}, and $r_{ps/pmma}$), and the thickness of the bottom and top layers, L and e, respectively. In the liquid/liquid bilayer system, the energy is dissipated in the less viscous layer when two liquids slide along each other. In our case, the viscosity of the bottom layer (n_{pmma} =1.2x10^5 Ns/cm^2) is much less than that of the upper PS layer (8.0 x 10^8 Ns/cm^2) at 190 °C.[32, 33] Therefore the bottom layer behaves like a liquid and the dewetting hole growth is governed by n_{pmma}. And if the bottom layer thickness (L) is smaller than the rim width

(l), the hole diameter (R) is proportional to $t^{2/3}$ according to equation 1 and then the velocities can be calculated by equation 2.

$$R = \left(\frac{\gamma^2 L^2 \theta}{\eta_e{}^2 e}\right)^{1/3} t^{2/3} \quad (1)$$

$$V = \left(\frac{\gamma^2 L^2 \theta}{\eta_e{}^2 e}\right)^{1/3} t^{-1/3} \quad (2)$$

Where γ is the effective surface tension and can be caculated by $1/\gamma = 1/\gamma_{ps} + 1/\gamma_{ps/pmma}$. θ is the equilibrium contact angle obtained from $\theta = \theta_A + \theta_B$ according to classical Neuman construction.[34] And θ_A is the equilibrium apparent contact angle while θ_B is the Neuman angle below the liquid/liquid interface. θ_B is allowed to be calculated from equation 3.

$$\gamma_{A/B} \sin\theta_B = \gamma_A \sin\theta_A \quad (3)$$

The contact angle θ_A between the droplets formed by the PS film and PMMA layer was directly measured using AFM and analyzed bythe slope of the profile close to the contact line.[35] From Figure 3.2i, we find unfilled bilayer sample has a contact angle of 4.3 ± 0.5°. The obtained contact angles are 3.6 ± 0.3 and 3.5 ± 0.4° for the samples filled with 0.04wt%graphene and 0.04wt%GO, respectively. θ_B can be calculated by substituting those values for θ_A and the corresponding values for γ_{ps}, $\gamma_{pmm/ps}$ into equation 3. The average hole diameters were measured from 5 to 10 holes and plotted as a function of the annealing time for calculating the viscosity of PMMA layer. Good fits are obtained for all experimental data with the theoretical power law, as shown in Figure 3.3 Compared with control sample, the dewetting hole growth rate decreases for both graphene and GO samples when the doping concentration increases.

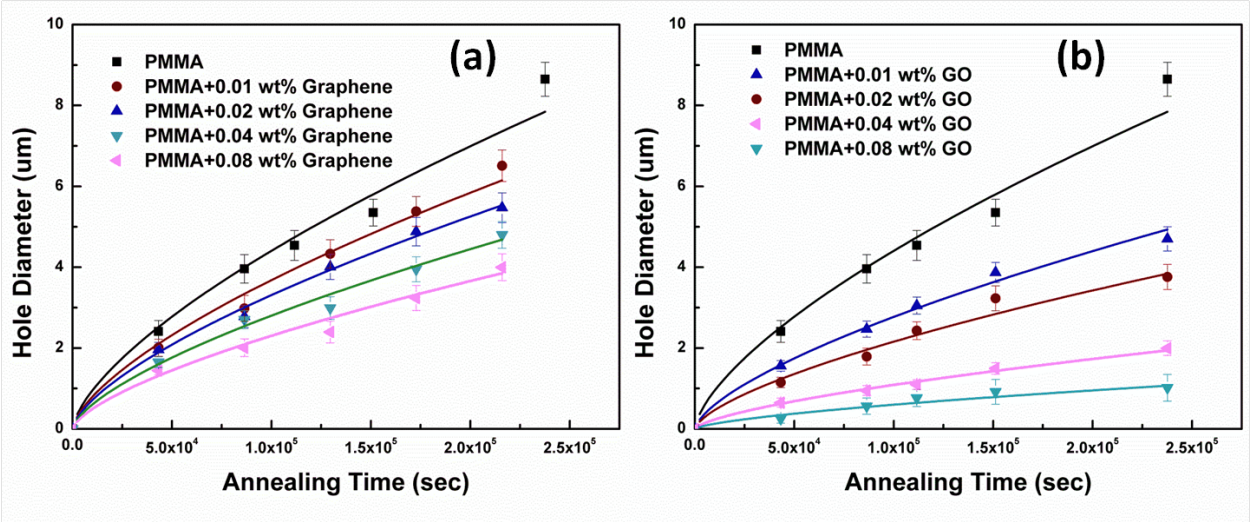

Figure 3. 3 Dewetting hole diameter of PS/PMMA bilayers as a function of annealing time and the concentration of graphene (a) and GO (b).

The effective viscosity (n_e) of the PMMA layers with different doping concentration of graphene and GO can be calculated by the fitting curves from equation 1. The obtained data were then plotted as a function of weight fraction of graphene and GO. From Figure 3.4, we can see the effective viscosity increase dramatically starting from 0.01wt%to 0.04wt%. According to the model used by Hough et al. and Du et al for describing the relation between viscosity and the doping ratio of the nanofillers,[36, 37] the sudden increase in the viscosity, followed by a plateau, can be interpreted as corresponding to a rheological percolation threshold above which the nanofillers physically impede the motion of polymers. The viscosity can be related to the mass fraction of nanofillers with a power law function.

$$\eta_e \sim (m - m_c)^{\alpha} \qquad (4)$$

Where m is the nanofiller mass fraction, mc is the threshold of percolation, and n is the percolation exponent. The solid line with percolation threshold value mc = 0.0063 wt% and α =0.33 gives a good fit to the data collected from graphene samples. In the case of GO loading, percolation threshold value mc is 0.0035 wt% while α increased to 0.98, suggesting that GO are much more effective than graphene at enhancing the viscoelastic response.

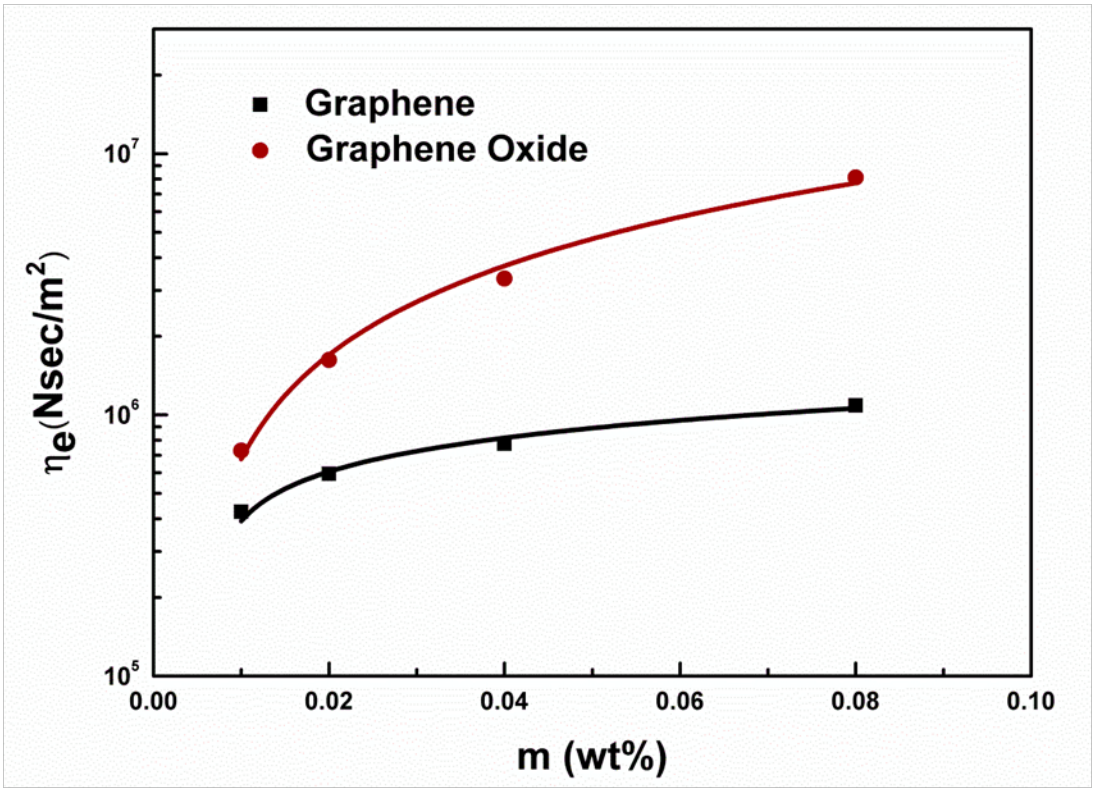

Figure 3. 4 Thin film viscosity derived from dewetting measurement as a function of the doping concentration of graphene and GO.

3.3.2 Interdiffusion Behavior

Neutron reflectivity is used to investigate the effect of graphene and GO on the tracer diffusion coefficient of the polymer chains. We started with simple bilayer geometry, where a 40 nm thick layer of deuterated PMMA (dPMMA) was first spun-cast on an HF etched silicon wafer and covered with another layer of PMMA floated from the surface of a distilled water bath. For experimental samples, two types of bilayers samples were investigated: one in which the graphene or GO was added to the dPMMA layer, another where the graphene or GO was added to the PMMA layer. All samples were annealed above the glass transition temperature of PMMA for different time. The neutron reflectivity data are shown in Figure 3.5, together with the SLD profiles that provided the best fits to the experimental data. The reflectivity data shows a few distinct fringes with a periodicity corresponding to the thickness of the deuterated bottom layer before annealing. The initial interface is sharply defined according the fitted SLD profile. As the

annealing time increases, the interface of the bilayer turns to broaden until dPMMA has diffused uniformly into both layers when a uniform frequency becomes visible in reflectivity profile.

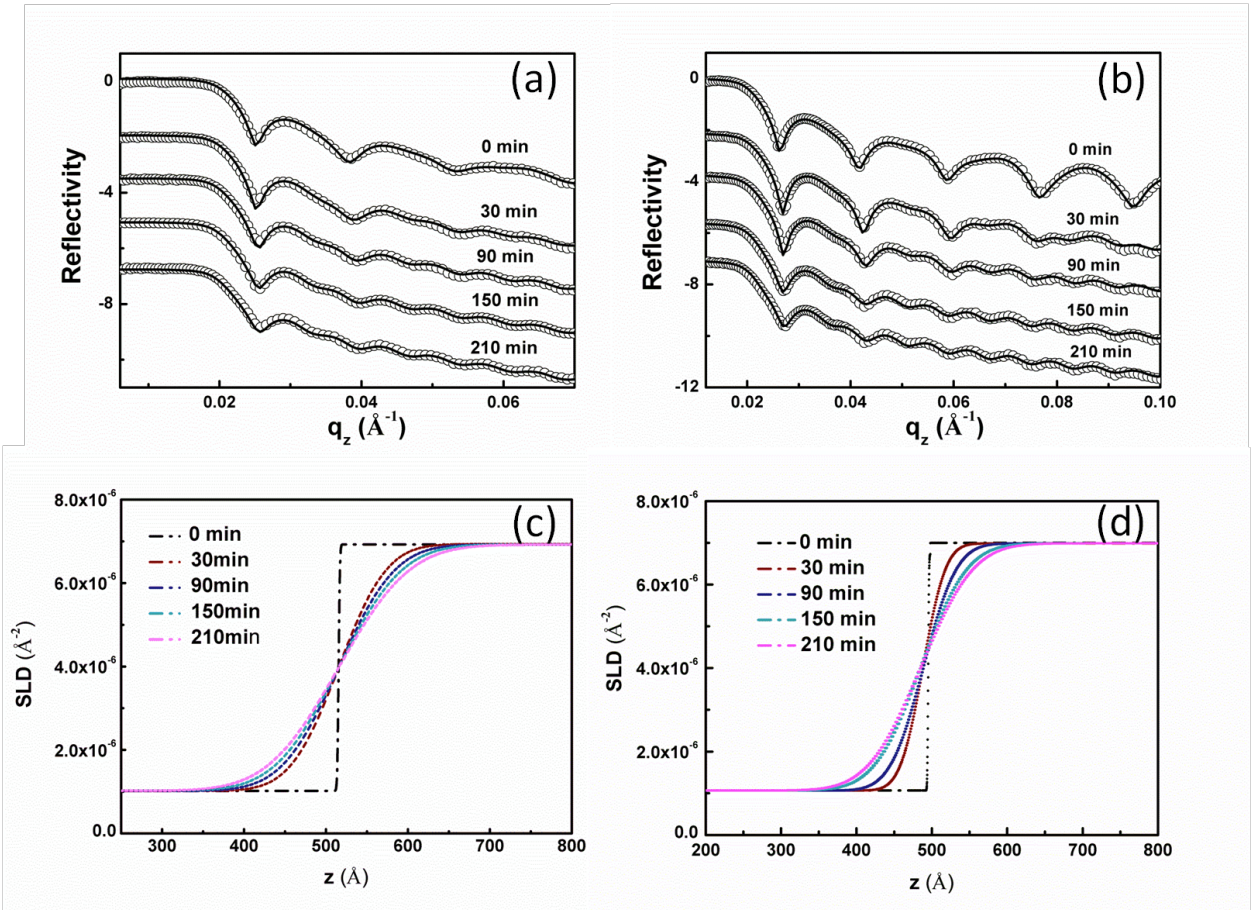

Figure 3. 5 Typical neutron reflectivity data from the PMMA/dPMMA bilayer films with different nanofillers in the bottom layer annealed at 138 °C as a function of time (a) with 0.1 wt% of graphene, (b) with 0.02 wt% of GO. The solid lines are the best fits to data. Consecutive reflectivities have been offset from each other for clarity. The corresponding scattering length density profiles as a function of the annealing time are shown in (c) for graphene and (d) for GO.

In the case of the Fickian diffusion,[38] the diffusion coefficient (D) can be related with the interface thickness and corresponding annealing time, as shown in in equation 5.

$$D = (\Delta\sigma/t^{1/2})^2/4 \quad (5)$$

Where t is the annealing time and $\Delta\sigma$ can be obtained from $\Delta\sigma = (\sigma_t^2 - \sigma_0^2)^{1/2}$, where σ_t is interfacial roughness and σ_0 is initial roughness of the interface. In order to calculate D, $\Delta\sigma$was

plotted as a function of the square root of annealing time for the PMMA/dPMMA bilayer samples unfilled and filled with 0.1wt%graphene and 0.02wt%GO in either top or bottom layers in Figure 3.6, where we find good linear fits applied in all cases. The diffusion coefficient D is determined from the slope of the fitted and tabulated in Table 3.1. While D is unaffected by the addition of graphene, GO significantly decreases the diffusion coefficient with only 0.02wt%at the same annealing temperature. This can be explained by the stronger interaction between PMMA with GO, which is supported by contact angle measurement as shown in Figure 3.7. The Si wafers covered with graphene and GO nanoparticles were prepared and then PMMA droplets were melted on the top of them for contact angle measurement. The SEM images indicate that the graphene and GO nanoparticles produce uniform multilayer films that fully cover the Si wafers. The contact angles for PMMA on graphene and GO layer are 68.33 ± 2.24 ^{O} and 32.98 ± 2.16 ^{O}, respectively. Compared with graphene, the smaller contact angle between PMMA and GO suggests that PMMA has a higher affinity for GO.

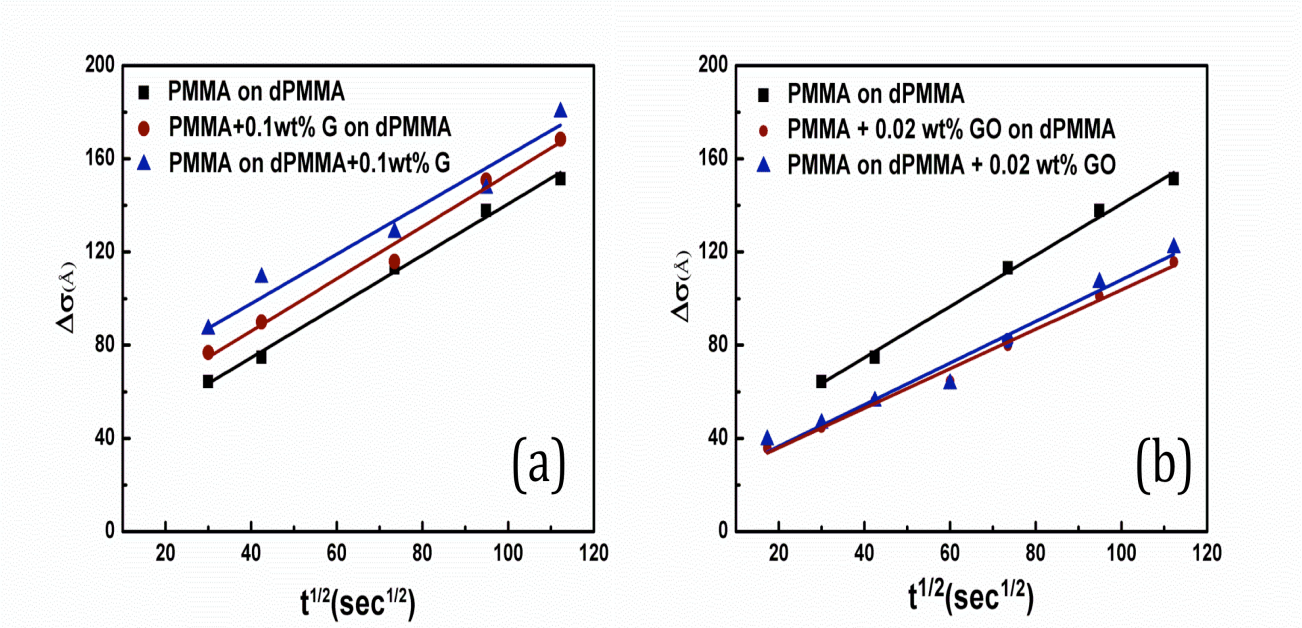

Figure 3. 6 The interface roughness plotted as a function of the square root of the annealing time at 150 °C for the PMMA/dPMMA bilayer films unfilled and filled with 0.1 wt% of graphene (a) and 0.02 wt% of GO (b).

Materials	Diffusion coefficient (x 10^{-15} cm^2/s)
PMMA on D-PMMA	3.03
PMMA+0.1G on D-PMMA	3.14
PMMA on D-PMMA+0.1G	2.81
PMMA+0.02%GO on D-PMMA	1.81
PMMA on D-PMMA+0.02%GO	1.94

Table 3. 1 Summary of the Diffusion Coefficients (D) of PMMA/dPMMA Bilayers unfilled and filled with graphene and GO

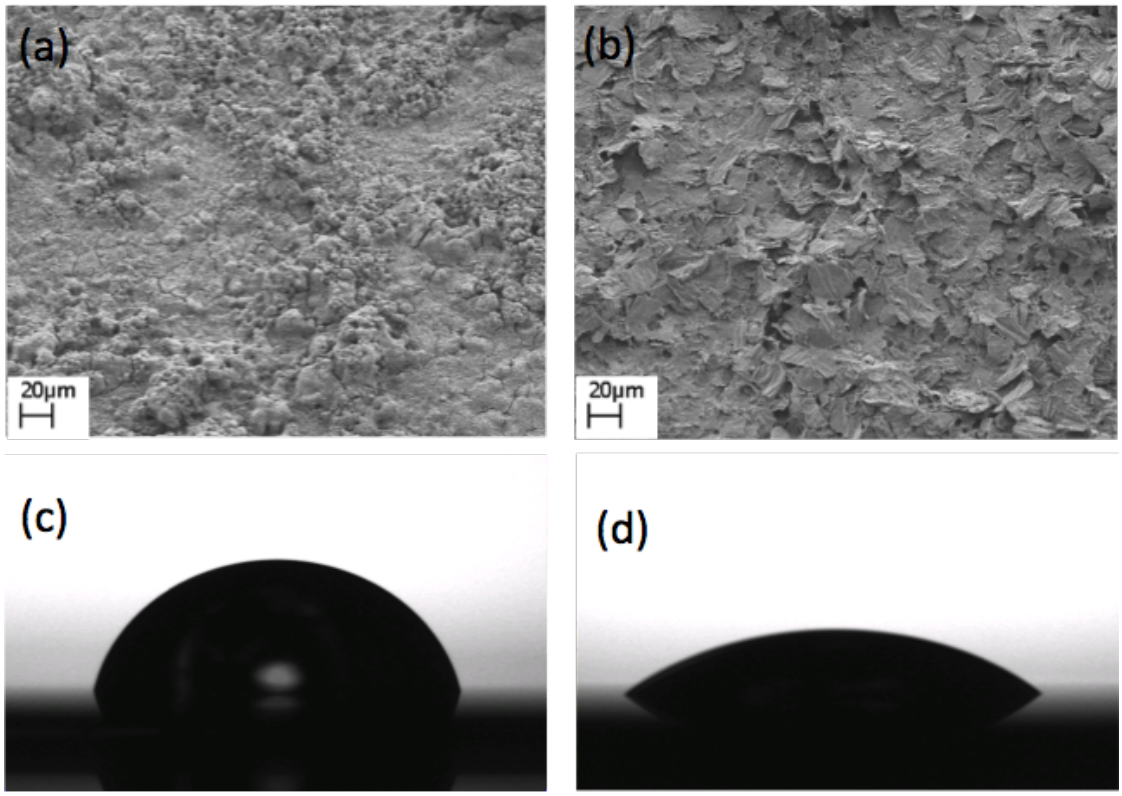

Figure 3. 7 SEM images of Si wafer covered with different nanoparticles: (a) graphen and (b) GO. Contact angle images of PMMA droplets on each nanoparticle layer: (c) PMMA on graphene, (d) PMMA on GO

3.4 Conclusion

We have investigated the effect of graphene and GO on the long-ranged motion and single chain dynamics of polymer thin films. In the dewetting experiment where long-ranged motion occurs, GO is more effective than graphene at stabilizing the polymer films against dewetting. The same trend was also observed for the single chain dynamics of PMMA film. The tracer diffusion coefficient was reduced by addition of GO while it was unaffected by the presence of the graphene nanoparticles. Those effects are caused by the more favorable interaction of GO with the polymer thin film, which is supported by the contact angle measurement.

Reference

1. Tian, H.-C.; Liu, J.-Q.; Wei, D.-X.; Kang, X.-Y.; Zhang, C.; Du, J.-C.; Yang, B.; Chen, X.; Zhu, H.-Y.; NuLi, Y.-N.; Yang, C.-S. Graphene oxide doped conducting polymer nanocomposite film for electrode-tissue interface. *Biomaterials* 2014, 35, 2120-2129.

2. Bai, H.; Li, C.; Shi, G. Functional Composite Materials Based on Chemically Converted Graphene. *Adv. Mater.* 2011, 23, 1089-1115.

3. Hu, K.; Kulkarni, D. D.; Choi, I.; Tsukruk, V. V. Graphene-polymer nanocomposites for structural and functional applications. *Prog. Polym. Sci.* 2014, 39, 1934-1972.

4. Wang, S.; Li, H.; Li, D.; Xu, T.; Zhang, S.; Dou, X.; Wu, L. Noncovalent Functionalization of Graphene Nanosheets with Cluster-Cored Star Polymers and Their Reinforced Polymer Coating. *ACS Macro Letters* 2015, 4, 974-978.

5. Geim, A. K.; Novoselov, K. S. The rise of graphene. *Nat. Mater.* 2007, 6, 183-191.

6. Potts, J. R.; Dreyer, D. R.; Bielawski, C. W.; Ruoff, R. S. Graphene-based polymer nanocomposites. *Polymer* 2011, 52, 5-25.

7. Kuilla, T.; Bhadra, S.; Yao, D.; Kim, N. H.; Bose, S.; Lee, J. H. Recent advances in graphene based polymer composites. *Prog. Polym. Sci.* 2010, 35, 1350-1375.

8. Kim, H.; Abdala, A. A.; Macosko, C. W. Graphene/Polymer Nanocomposites. *Macromolecules* 2010, 43, 6515-6530.

9. Pham, V. H.; Dang, T. T.; Hur, S. H.; Kim, E. J.; Chung, J. S. Highly Conductive Poly(methyl methacrylate) (PMMA)-Reduced Graphene Oxide Composite Prepared by Self-Assembly of PMMA Latex and Graphene Oxide through Electrostatic Interaction. *ACS Appl. Mater. Interfaces* 2012, 4, 2630-2636.

10. Wang, G.; Zhuo, S.; Xing, W. Graphene/polyaniline nanocomposite as counter electrode of dye-sensitized solar cells. *Mater. Lett.* 2012, 69, 27-29.

11. Yong, Y.-C.; Dong, X.-C.; Chan-Park, M. B.; Song, H.; Chen, P. Macroporous and Monolithic Anode Based on Polyaniline Hybridized Three-Dimensional Graphene for High-Performance Microbial Fuel Cells. *ACS Nano* 2012, 6, 2394-2400.

12. Wang, H.; Hao, Q.; Yang, X.; Lu, L.; Wang, X. Graphene oxide doped polyaniline for supercapacitors. *Electrochem. Commun.* 2009, 11, 1158-1161.

13. Lin, Y.; Dong, X.; Liu, S.; Chen, S.; Wei, Y.; Liu, L. Graphene–Elastomer Composites with Segregated Nanostructured Network for Liquid and Strain Sensing Application. *ACS Appl. Mater. Interfaces* 2016, 8, 24143-24151.

14. Jang, B. Z.; Zhamu, A. Processing of nanographene platelets (NGPs) and NGP nanocomposites: a review. *Journal of Materials Science* 2008, 43, 5092-5101.

15. Zhang, X.; Samorì, P. Graphene/Polymer Nanocomposites for Supercapacitors. *ChemNanoMat* 2017, 3, 362-372.

16. Cao, Y.; Zhang, J.; Feng, J.; Wu, P. Compatibilization of Immiscible Polymer Blends Using Graphene Oxide Sheets. *ACS Nano* 2011, 5, 5920-5927.

17. You, F.; Wang, D.; Li, X.; Liu, M.; Dang, Z.-M.; Hu, G.-H. Synthesis of polypropylene-grafted graphene and its compatibilization effect on polypropylene/polystyrene blends. *J. Appl. Polym. Sci.* 2014, 131, n/a-n/a.

18. Armstrong, N. R.; Wang, W.; Alloway, D. M.; Placencia, D.; Ratcliff, E.; Brumbach, M. Organic/Organic′ Heterojunctions: Organic Light Emitting Diodes and Organic Photovoltaic Devices. *Macromol. Rapid Commun.* 2009, 30, 717-731.

19. Lu, G.; Usta, H.; Risko, C.; Wang, L.; Facchetti, A.; Ratner, M. A.; Marks, T. J. Synthesis, Characterization, and Transistor Response of Semiconducting Silole Polymers with Substantial Hole Mobility and Air Stability. Experiment and Theory. *J. Am. Chem. Soc.* 2008, 130, 7670-7685.

20. Helgesen, M.; Sondergaard, R.; Krebs, F. C. Advanced materials and processes for polymer solar cell devices. *J. Mater. Chem.* 2010, 20, 36-60.

21. Singh, J.; Agrawal, K. K. Polymeric Materials for Contact Lenses. *Journal of Macromolecular Science, Part C* 1992, 32, 521-534.

22. Bandyopadhyay, D.; Douglas, J. F.; Karim, A. Influence of C60 Nanoparticles on the Stability and Morphology of Miscible Polymer Blend Films. *Macromolecules* 2011, 44, 8136-8142.

23. Xue, L.; Han, Y. Inhibition of dewetting of thin polymer films. *Prog. Mater Sci.* 2012, 57, 947-979.

24. Cowie, J. M. G. *Polymers: chemistry and physics of modern materials*.

25. Reiter, G.; Schultz, J.; Auroy, P.; Auvray, L. Improving adhesion via connector polymers to stabilize non-wetting liquid films. *Europhys. Lett.* 1996, 33, 29-34.

26. Siegel, R. W. Synthesis and properties of nanophase materials. *Materials Science and Engineering: A* 1993, 168, 189-197.

27. Sirringhaus, H.; Tessler, N.; Friend, R. H. Integrated optoelectronic devices based on conjugated polymers. *Science* 1998, 280, 1741-1744.

28. Wang, W. C.; Vora, R. H.; Kang, E. T.; Neoh, K. G.; Ong, C. K.; Chen, L. F. Nanoporous Ultra-Low-κ Films Prepared from Fluorinated Polyimide with Grafted Poly(acrylic acid) Side Chains. *Adv. Mater.* 2004, 16, 54-57.

29. Koo, J.; Shin, K.; Seo, Y.-S.; Koga, T.; Park, S.; Satija, S.; Chen, X.; Yoon, K.; Hsiao, B. S.; Sokolov, J. C.; Rafailovich, M. H. Stabilizing Thin Film Polymer Bilayers against Dewetting Using Multiwalled Carbon Nanotubes. *Macromolecules* 2007, 40, 9510-9516.

30. Wyart, F. B.; Martin, P.; Redon, C. Liquid/liquid dewetting. *Langmuir* 1993, 9, 3682-3690.

31. Kim, T.-H.; Kim, H.; Choi, K.-I.; Yoo, J.; Seo, Y.-S.; Lee, J.-S.; Koo, J. Graphene Oxide Monolayer as a Compatibilizer at the Polymer–Polymer Interface for Stabilizing Polymer Bilayer Films against Dewetting. *Langmuir* 2016, 32, 12741-12748.

32. Fuchs, K.; Friedrich, C.; Weese, J. Viscoelastic Properties of Narrow-Distribution Poly(methyl methacrylates). *Macromolecules* 1996, 29, 5893-5901.

33. Li, C.; Koga, T.; Li, C.; Jiang, J.; Sharma, S.; Narayanan, S.; Lurio, L. B.; Hu, X.; Jiao, X.; Sinha, S. K.; Billet, S.; Sosnowik, D.; Kim, H.; Sokolov, J. C.; Rafailovich, M. H. Viscosity Measurements of Very Thin Polymer Films. *Macromolecules* 2005, 38, 5144-5151.

34. Slep, D.; Asselta, J.; Rafailovich, M. H.; Sokolov, J.; Winesett, D. A.; Smith, A. P.; Ade, H.; Anders, S. Effect of an Interactive Surface on the Equilibrium Contact Angles in Bilayer Polymer Films. *Langmuir* 2000, 16, 2369-2375.

35. Pack, S.; Kashiwagi, T.; Cao, C.; Korach, C. S.; Lewin, M.; Rafailovich, M. H. Role of Surface Interactions in the Synergizing Polymer/Clay Flame Retardant Properties. *Macromolecules* 2010, 43, 5338-5351.

36. Hough, L. A.; Islam, M. F.; Janmey, P. A.; Yodh, A. G. Viscoelasticity of single wall carbon nanotube suspensions. *Phys. Rev. Lett.* 2004, 93.

37. Du, F.; Scogna, R. C.; Zhou, W.; Brand, S.; Fischer, J. E.; Winey, K. I. Nanotube Networks in Polymer Nanocomposites: Rheology and Electrical Conductivity. *Macromolecules* 2004, 37, 9048-9055.

38. Doi, M.; Edwards, S. F. *The theory of polymer dynamics*. Clarendon Press ; Oxford University Press: Oxford Oxfordshire New York, 1986; p xiii, 391 p.

Chapter 4. Conjugated Polymer/Fullerene Hybrid Fibers for Bulk-Heterojunction Organic Solar Cells

4.1 Introduction

Bulk heterojunction (BHJ) polymer solar cells are a field of intense interest due to their flexibility, low cost, and ease of processing.[1-4]The performance of these devices is known to be highly dependent on the morphology of the active layers,[5-9]and to critically suffer from unfavorable features such as isolated domains or dead ends.[4] Therefore a variety of methods have been explored to finely control such morphology, such as thermal annealing,[10-12] solvent annealing,[13, 14]self-assembly of columnar polymer phases,[15] and micropatterning.[16]Recently, a different route has been developed based on the use of organic nanofibers to optimize the donor-acceptor interface morphology.Polymer nanorods[12]and nanofibers,[8] prepared by melt-assisted wettingor by a variety of thermally-assisted processing techniques[17-19],have been shown to increase hole mobility, inducing higher mesoscopic order and crystallinity, enhanced donor-acceptor interfaces, and ultimately leading to better device performance compared with polymer films, due to the formed nanoscale and possibly interpenetrating network of fibrillar components. Systems investigated so far have been mostly limited to melts or self-assembled nanostructures made of polythiophene donors, such as core-shell nanorods or layers embedding fibrils of poly(3-hexylthiophene) or poly(3-butylthiophene) and the acceptor phenyl-C_{61}-butyric acid methyl ester (PCBM).[18-20] Developing processing methods which can extend the range of used conjugated polymers and offer higher throughput are therefore strongly desirable, in view of exploiting networked fibrillar morphologies to enhance the performance of BHJ solar cells at larger scale.

Electrospinning is a straightforward technology for the realization of continuous fibers with sub-μm diameter through the application of a high voltage bias to polymer solutions,[21, 22] This process enables the production of non-wovens made of fibers with

high surface-area-to-volume ratio, which can be deposited in random networks or in uniaxially aligned arrays with three-dimensional porosity.Due to its versatility in terms of usable polymers and blends and to its good throughput, electrospinning shows high potential as method to tailor the microstructure and the composition of active materials for polymer optoelectronic devices, including solar cells, in a controlled way.[23]Demonstrated applications include field-effect transistors[24, 25]and luministors,[26]rechargeable batteries,[27]energy harvesters,[28, 29] light-emitting devices[30, 31]and nanopatterned lasers.[32] Electrospun photovoltaic materials would ultimately lead to the development of so-called solar cloths[33] for smart textile technologies. In addition, organic fibers with diameters matching the wavelength of solar light can exhibit exceptional light-scattering performances, as recently found in insect scales formed by interconnected filaments of chitin[34], thus possibly enhancing the coupling of light into the absorbing regions of layered devices. Unfortunately, electrospinning conjugated polymers is frequently difficult due to the generally poor viscoelastic behavior of the solutions, which corresponds to a low amount of molecular entanglements, and to the limited solubility of these compounds. Hence the use of electrospinning methods to produce fibrillar components in BHJ polymer solar cells and modules has been only rarely attempted.[35-39] Recently it was shown that electrospinning can be carried out with a few photoactive polymers, upon encasing them in an inert/insulating polymer in a core-shell fiber configuration.[36, 38] This method though also proved to be difficult since the shell polymer must first be removed for the device to function, and this step could potentially damage the surface of the remaining functional fibers. Much wider efforts have been instead directed to the realization of dye-sensitized solar cells exploiting electrospun materials, as discussed ina recent review.[40]

Here we focus on polymer blends to facilitate the electrospinning process. We have previously demonstrated that addition of a secondary polymer component is beneficial to maintain the structure of BHJ solar cell films, despite the fact that the second component is not photoactive.[15] Here we report on electrospun poly[2-methoxy-5-(2-ethylhexyloxy)-1,4 phenylenevinylene]/ polyvinylpyrrolidone/PCBM (MEH-PPV/PVP/PCBM) blend fibers which are stable, easily produced, and yet photoactive, and which significantly

improve the performance of BHJ solar cells. Fibers are incorporated in the device active layer upon deposition of a fully solubilized poly(3-hexylthiophene-2,5-diyl)/PCBM (P3HT/PCBM) backfill layeron top. Partial redissolution of the electrospun fibers occurs at the backfill layer deposition, however the structural coherence and shape of the fibers are largely maintained in solution-processed multilayer device architectures. Therefore, the three-dimensional entangled fiber network serves as a template for P3HT/PCBM and the resulting overall morphology of the active layer leads to higher short-circuit current density (J_{sc}) and fill factor (*FF*) values compared to thin-film devices without electrospun fibers.

4.2. Experiment

4.2.1 Materials

MEH-PPV (Mw=150-250 KDa) is purchased from Aldrich. PCBM is provided by SES research and PVP (Mw=1,300 KDa) by Alfa Aesar. Chlorobenzene, chloroform and P3HT (Mw 54-75 KDa) are obtained from Sigma-Aldrich. All materials are used without further purification.

4.2.2 Fabrication and Characterization of the Nanofibers

The solution for electrospinning is made of MEH-PPV/PVP/PCBM dissolved in chloroform at a concentration of 15/15/10 mg/mL, respectively. It is then stirred at room temperature for 12 hours to allow for complete polymer dissolution, loaded in a syringe with a 21 gauge stainless steel needle, and injected through the needle at constant flow rate (0.5 mL/h) by a syringe pump (Harvard Apparatus, Holliston, MA). A 8 kV voltage is applied at the needle using a high-voltage power supply (EL60R0.6–22, Glassman High Voltage, High Bridge, NJ). Electrospinning is carried out in ambient atmosphere, and fibers are collected on square (1.5×1.5 cm^2) polymer/TiO_2/indium tin oxide (ITO)/glass substrates mounted on a rotating disk collector (4000 rpm) at a distance of 15 cm from the needle. A cross-bar pattern of fibers is obtained by depositing fibers along

two mutually perpendicular directions, rotating the substrates by 90° after the first deposition stage, as inspected by scanning electron microscopy (SEM, FEI, Hillsboro, Figure 4.1). Prior to electrospinning, the substrates are carefully prepared as described in the next Section.

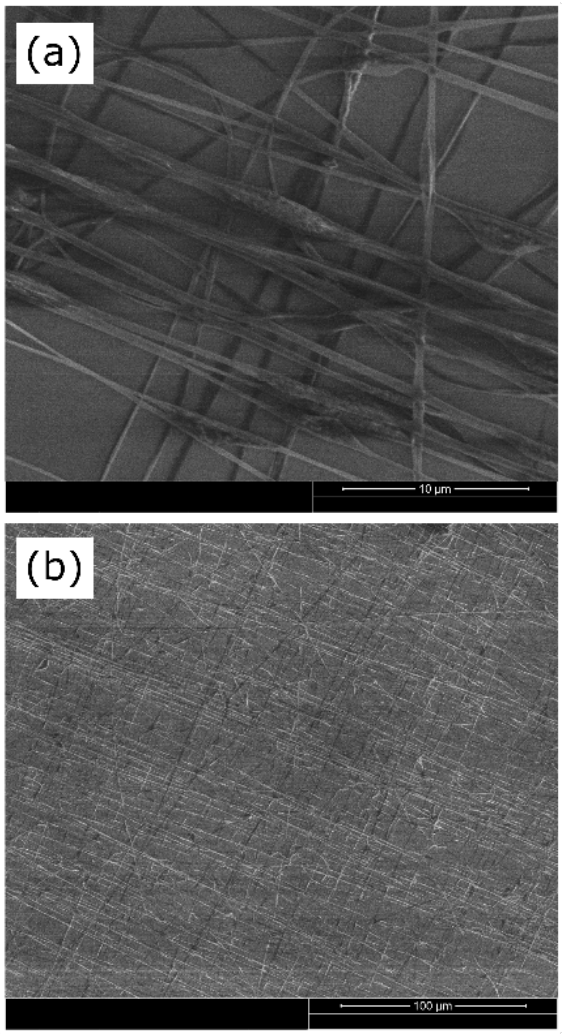

Figure 4. 1 SEM micrographs of electrospun MEH-PPV/PVP/PCBM fibers in cross-bar configuration, imaged at different magnifications. Locally rough surface, suggesting phase-separation occurring in the blend during electrospinning, is visible in the thicker regions in the fibers in (a). Images also show that fibers are superimposed at different heights on the substrate, thus generating a truly three-dimensional network.

UV-Visible absorption spectra are obtained with a Thermo Scientific Evolution 200 UV-VIS Spectrophotometer. The photoluminescence (PL) properties of the fibers are examined in micro-PL mode by using a confocal microscopy system, composed of an inverted microscope (Eclipse Ti, Nikon) and a laser scanning head (A1R MP, Nikon). To this aim, samples are excited by an Ar^+ laser (λ_{exc}=488 nm) through a 20× objective (numerical aperture = 0.5), while the intensity of the fluorescence, collected by the same excitation objective, is measured by using a spectral detection unit equipped with a multi-anode photomultiplier (Nikon). This allows spatially-resolved spectra and fluorescence images to be collected.

PL quantum yield measurements are performed following the procedure in previous report.[41]Fiber samples deposited on quartz substrates were positioned in an integrating sphere and excited by a UV light emitting diode (LED, peak emission wavelength = 300 nm and linewidth = 18 nm). The excitation and emission optical signals are collected by an optical fiber, coupled to a monochromator (iHR320, Jobin Yvon) and measured by a charge coupled device camera (Symphony, Jobin Yvon).

Attenuated Total Reflectance Fourier Transform-Infrared (FTIR) spectroscopy is performed on electrospun fibers using a spectrometer (Spectrum 100, Perkin Elmer, Waltham, MA) equipped with a ZnSe crystal for coupling (Perkin Elmer).

Images of the surface topography and electrical conductivity are also obtained using a Bruker Dimension Icon atomic force microscope (AFM, Multimode, Bruker) operating in PeakForce tunneling mode.

4.2.3 BHJ Polymer Solar Cell Devices

ITO-coated glass is polished in UV/ozone for 10 min to remove any organic impurity. A TiO_2 solution is prepared according to previous reports.[42] Briefly, the solution is obtained by dissolving 1mL $Ti(OC_4H_9)_4$ in 10 mL ethanol, followed by adding 1 mL of

CH_3COOH, then 1 mL of acetylacetone, and 1 ml of deionized water. The solution is stirred at room temperature for 30 min before each reagent is added. A 30 nm thick TiO_2 layer is then spun onto ITO at 3000 rpm for 20 s and baked in air at 400°C for 2 hours on a hot plate. To maximize adhesion of fibers, a ~10 nm thick film of MEH-PPV/PVP/PCBM is spin-cast on the TiO_2 layer at 6000 rpm for 30 s. MEH-PPV/PVP/PCBM fibers are then electrospun as described above. A solution of P3HT/PCBM (15/9 mg/mL in chlorobenzene) is used to interconnect the fibers upon spin-coating at 1000 rpm for 30 s. Samples are then annealed at 150 °C for 10 min in a vacuum oven. Finally, the devices are completed by thermal evaporation of 8 nm MoO_3 and 100 nm Ag electrode with a Kurt J. Lesker PVD 75 vacuum deposition system at Brookhaven National Laboratory. Control devices are prepared with the same procedure but without electrospun fibers.The performance of so-realized solar cells is tested by a 150 W solar simulator (Oriel) with an AM 1.5G filter for solar illumination. The light intensity is adjusted at 100 mW cm^{-2} by a calibrated thermopile detector (Oriel).

4.2.4 Light Scattering by Non-Spherical Particles in the T-matrix Formalism

Light scattering calculations for the developed material are carried out in the T-matrix formalism. We consider the fiber structure as composed of aggregates of spheres embedded into a homogeneous, isotropic, indefinite medium. The optical properties of the subunit spheres and the surrounding medium are calculated using the Bruggeman description.[43] The incident field is the polarized plane wave (whose results are eventually averaged over the in-plane polarization angle), hence the total field outside the particle is the sum of the incident and scattered field. The scattered field is obtained applying the boundary conditions across the surface of each particle of the structure, linking the internal and external fields. The scattering problem is solved by the T-matrix method,[44-49] based on the definition of a linear operator relating the incident field to the scattered field.[44] In brief, the starting point of the method is the field expansion in terms of the spherical multipole fields, i.e., the vector solutions of the Maxwell equations in a homogeneous medium that are simultaneous eigenfunctions of the angular momentum

and the parity operators. The operator S, called transition operator, is introduced thanks to the linearity of the Maxwell equations and of the equations expressing the boundary conditions across the surface of the particle. The representation of the operator S on the basis of the spherical multipole fields gives the T-matrix whose elements, $S_{lml'm'}^{(pp')}(r,k)$, (with p parity index, l and m angular momentum indices) contain all the information about the scattering process, but are independent of the state of polarization of the incident field. Here, we use the cluster model[45-47] to get the scattering properties of fibrous mats embedded in a surrounding medium. The cluster model is a special case since the T-matrix approach solves the scattering problem by an aggregate (cluster) of spheres without resorting to any approximation.[47] This is highly useful since it allows to simulate many situations of practical interest where one deals with non-spherical scatters. We also highlights that in order to calculate the T-matrix of a cluster one has to solve a linear system of equations with, in principle, infinite order. Thus, the system must be truncated to some finite order by including into the multipole expansions terms up to this truncation, chosen so to ensure the convergence of the calculations. As a consequence, the computational demand for these calculations increases with the cube of the number of spheres.[48-50]

4.3. Results and discussion

4.3.1 Optical Properties of Nanofiber Sample

The fabrication process of a BHJ solar cell embedding electrospun MEH-PPV/PVP/PCBM fibers is summarized in Fig. 4.2. A backfill layer of fully solubilized P3HT/PCBM is spin-cast onto the top of the nanofibrous layer, thus interconnecting the electrospun fibers and avoiding short circuit contacts of the two electrodes which would be likely to occur due to the highly porous nature of the network of filaments. Finally, MoO_3 and Ag are deposited as electron blocking layer and anode, respectively. For the deposition of the nanofibrous layers, electrospinning is optimized to provide a three-dimensional and interconnected structure made of MEH-PPV fibers blended with PCBM. To overcome the poor spinnability of pristine MEH-PPV, due to its limited molecular weight (150-250 KDa) and generally poor viscoelastic behaviour in solution, an easily spinnable component given by PVP is added to the solution. MEH-PPV and PVP are blended at a 1:1 (w:w) relative concentration, which is found to lead to fiber formation with stable electrified jets and good efficiency. In addition, we tune the density of the nanofibrous network to obtain a given degree of coverage onto the device surface. A deposition time of a few minutes is used to obtain a thickness ranging from one to a few superimposed layers of fibers. Differently from previous works,we do not employ sacrificial sheaths in core-shell nanofibers, which would need additional processing steps to be removed, but instead use a unique blend system relying on percolative paths for internal charge transport. The morphology of MEH-PPV/PVP/PCBM electrospun fibers, shown in Fig. 4.1, highlights that three-dimensional nonwoven networks are formed, where fibers are uniformly dispersed and exhibit ribbon-shape, and transversal size ~300-450 nm, with very rare beads over a large area. The domains observed on the fiber surface suggest phase separation of the different polymer components at scales (few tens of nm) well matching the typical exciton diffusion lengths in organics.

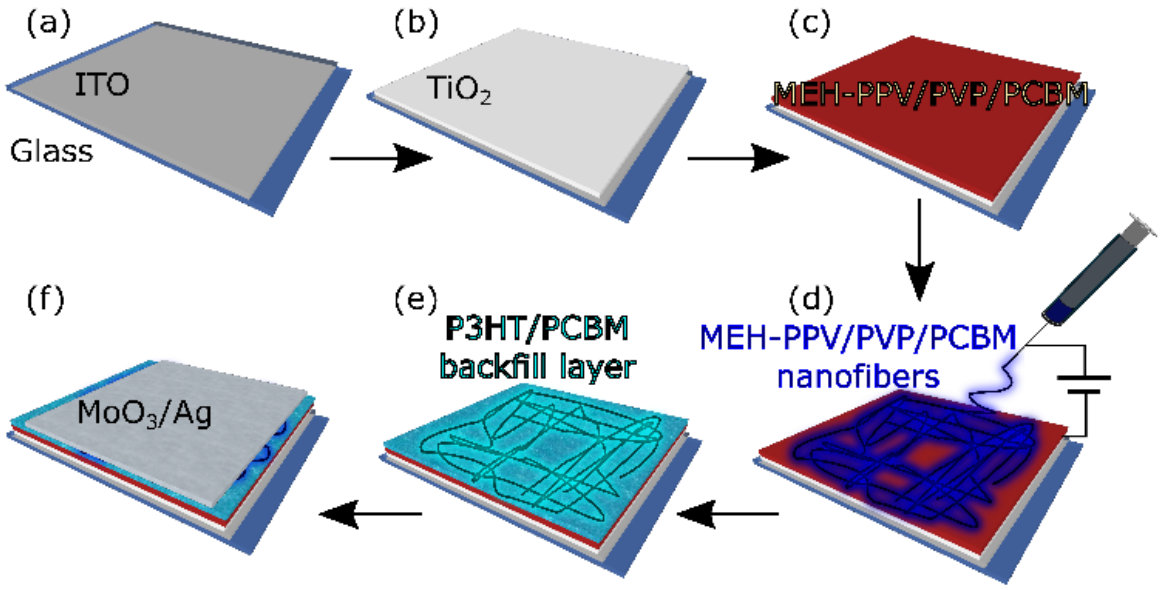

Figure 4. 2 Scheme of the process for realizing solar cell devices based on electrospun, MEH-PPV/PVP/PCBM nanofibers.The fibers are spun on ITO/glass substrates (a) following the deposition of a 30 nm thick TiO2 layer (b) and of a spin-cast MEH-PPV/PVP/PCBM film (c). After electrospinning, (d), P3HT/PCBM is spin-cast to define the template active layer, and the electron-blocking and top electrode are thermally evaporated (f).

FTIR spectra of electrospun MEH-PPV/PVP/PCBM fibers show a band peaked at 528 cm^{-1}, which is characteristic for the fullerene derivatives(Fig. 4.3)[51, 52]. More importantly, the presence of PCBM in these fibers and the formation of effective internal interfaces between the acceptor and the donor compounds in the organic fibers is supported by the reduction of the PL quantum yield found for fibers with fullerene compared to MEH-PPV/PVP fibers. Indeed, the PL quantum yield of the MEH-PPV/PVP fibers, measured by an integrating sphere and accounting for the number of emitted photons per incident photons, is 11±1%, decreasing by at least one order of magnitude (<1 %) upon fullerene addition. Furthermore, the PL spectrum of the MEH-PPV/PVP/PCBM fibers is blue-shifted by 10 nm, compared to MEH-PPV/PVP fibers (Fig. 4.4a). Such blue-shift is also found by measuring the spatially-resolved fluorescence spectra of the fibers by micro-PL, allowing us to collect PL maps with sub-micron spatial resolution (Fig. 4.4b,c). The uniform brightness along the fibers in the micrographs in Fig. 4.4b and 4.4c clearly indicates a homogeneous incorporation of MEH-PPV in the electrospun filaments. In particular, the

analysis of the spectra collected from different areas of the fiber samples evidence a substantial blue-shift of the average peak wavelength (by 12 nm, Fig. 4.4d,e) due to the presence of PCBM, together with a broadening of the peak wavelength distribution, featuring an increase of the full width at half maximum from 2 nm to 7 nm upon PBCM addition.

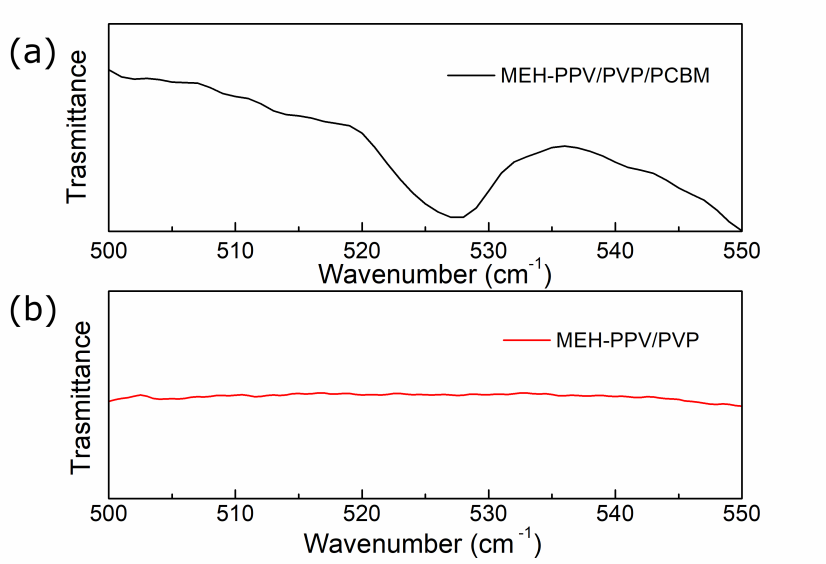

Figure 4. 3 FTIR spectrum in the 500-550 cm-1 region, for (a) MEH-PPV/PVP/PCBM fibers and (b) MEH-PPV/PVP fibers, highlighting the presence of the band peaked at 528 cm−1 upon fullerene doping.

Following photo-excitation, the emission properties of conjugated polymers, which are multi-chromophore systems composed by many active sub-units, are determined by energy migration, funneling the excitation toward those chromophores that have lower characteristic energies.[53] In pristine electrospun nanofibers made by conjugated polymers this process occurs on picosecond timescales, and it determines the emission to occur from the more extended and conjugated sub-units.[54]

The presence of PBCM and the formation of effective interfaces for dissociation of photogenerated excitons introduce additional nonradiative recombination pathways limiting the exciton migration and radiative recombination. This leads to blue-shifted emission and lower PL quantum yield, similarly to pristine samples with increased molecular disorder and aggregation.[54] Overall, these findings support the occurrence of

diffusion and dissociation of photogenerated excitons at interfaces formed within electrospun nanofibers.

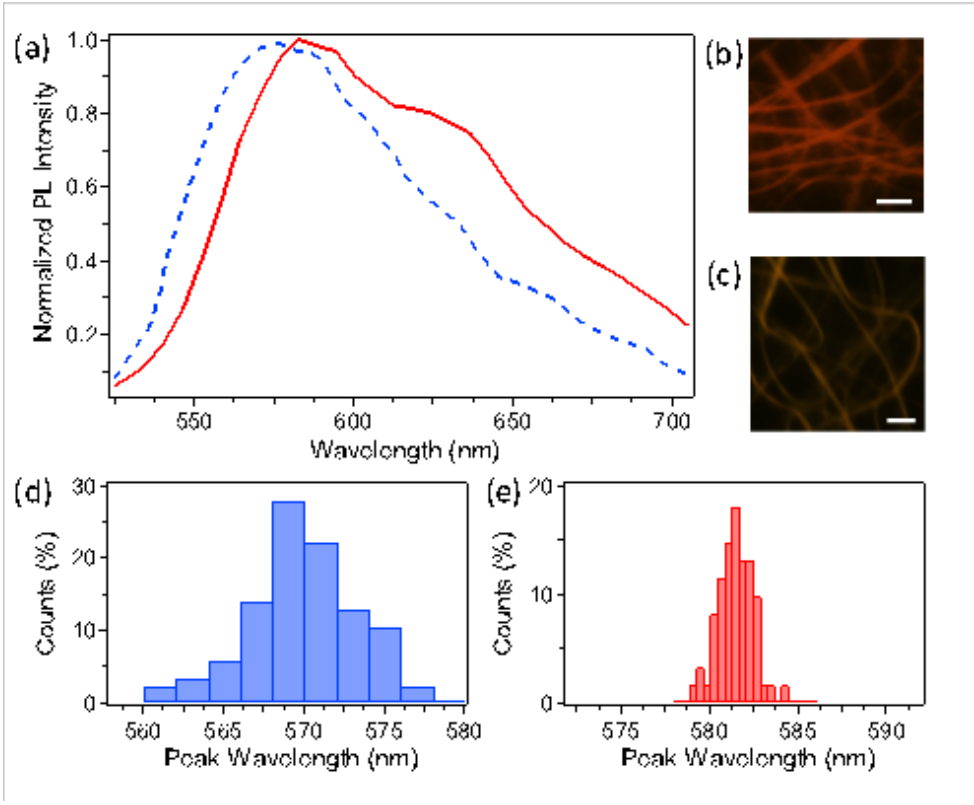

Figure 4. 4 (a) PL spectra of MEH-PPV/PVP nanofibers (red continuous line) and of MEH-PPV/PVP/PCBM nanofibers (blue dashed line). (b,c) Exemplary fluorescence maps of MEH-PPV/PVP and MEH-PPV/PVP/PCBM, respectively, measured by confocal microscopy. Scale bars: 10 µm.(d,e) Distribution of the peak emission wavelengths for MEH-PPV/PVP/PCBM and MEH-PPV/PVP nanofibers, respectively, obtained after measuring spatially-resolved fluorescence spectra. The spectra used for the analysis are averaged over a ~1 µm2 area along the length of fibers.

4.3.2 Morphology of the Active Layer

The morphology of the active layer surface as resulting from the fiber deposition is studied with lateral- force AFM (Fig. 4.5). It can be seen from Fig. 4.5a that the structural coherence of MEH-PPV/PVP/PCBM fibers is well maintained after depositing the P3HT/PCBM backfill layer. Though with partial flattening due to partial dissolution, the fiber network still serves as a templatefor the active layer (Fig. 4.5b). In this way a complex, double-heterojunction and tandem-resembling structure is kept in the active film. The layered structures create multiple donor-acceptor interfaces, which are formed in the fibers and in the backfill layer, respectively, and a unique PCBM component possibly promoting the development of percolative paths for electrons across regions realized with different blends. In Fig. 4.5c and 4.5d we show a magnified view of the region highlighted by the squared in Fig. 4.5a and 4.5b, respectively. Though not visible in the topographic images due to their small heights (~2 nm), PCBM inclusions can be clearly seen in the friction image (Fig. 4.5d), where they appear slightly darker or harder than their surroundings. The PCBM is arranged in long streaks that run along the length of the fiber. The PCBM that we view also lies directly on the surface of the fiber, since the friction mode scans are only sensitive to differences in mechanical or adhesion surface forces. Imaging the electrospinning process using fast X-ray analysis, it was previously shown that particle inclusions self-assemble in long streaks that run along the length of fiber, and delineate the stream lines of the electrospining jet. In order to maintain lamellar flow in the viscous stream, particle inclusions are also pushed towards the surface of the stream, where the deformation they cause is minimized.[55] Along the jet, due to the dominant effect of axial stretching accompanied by lateral contraction,the particles tend to be segregated towards the surface of the fibers in the as spun samples. A cartoon of the PCBM distribution in the electrospun fibers, in both side and top view is shown in Fig. 5e. If the PCBM concentration is sufficiently high a percolative network forms on the surface of the fiber, which might be very effective in increasing the current of a BHJ photovoltaic device. We also utilize Tunnelling (TUNA)-AFM to investigate the fiber conductivity. Fig 4.5f displays a region of an electrospun MEH-PPV/PVP/PCBM filament deposited on the blend film. The corresponding current map for zero bias

highlights no significant difference between the fiber and the surrounding film. Upon increasing the applied voltage to 2V, the fiber features are brought back and match well with the topography image (Fig. 4.5g). The current detected from the fiber area (about 1.5 fA) is lower than that from film due to the higher serial resistance. Indeed, the ratio of the measured current values for the fiber and the surrounding layer (~25) well agrees with the ratio of the corresponding thickness in the two probed areas. Overall, these results indicate a homogeneous charge transport behavior for the adhesion film and the fibers along their transversal direction, and conductivity values ($1.02\text{-}1.34\times10^{-7}$ S/m) adequate for optoelectronic applications, such as solar cells.

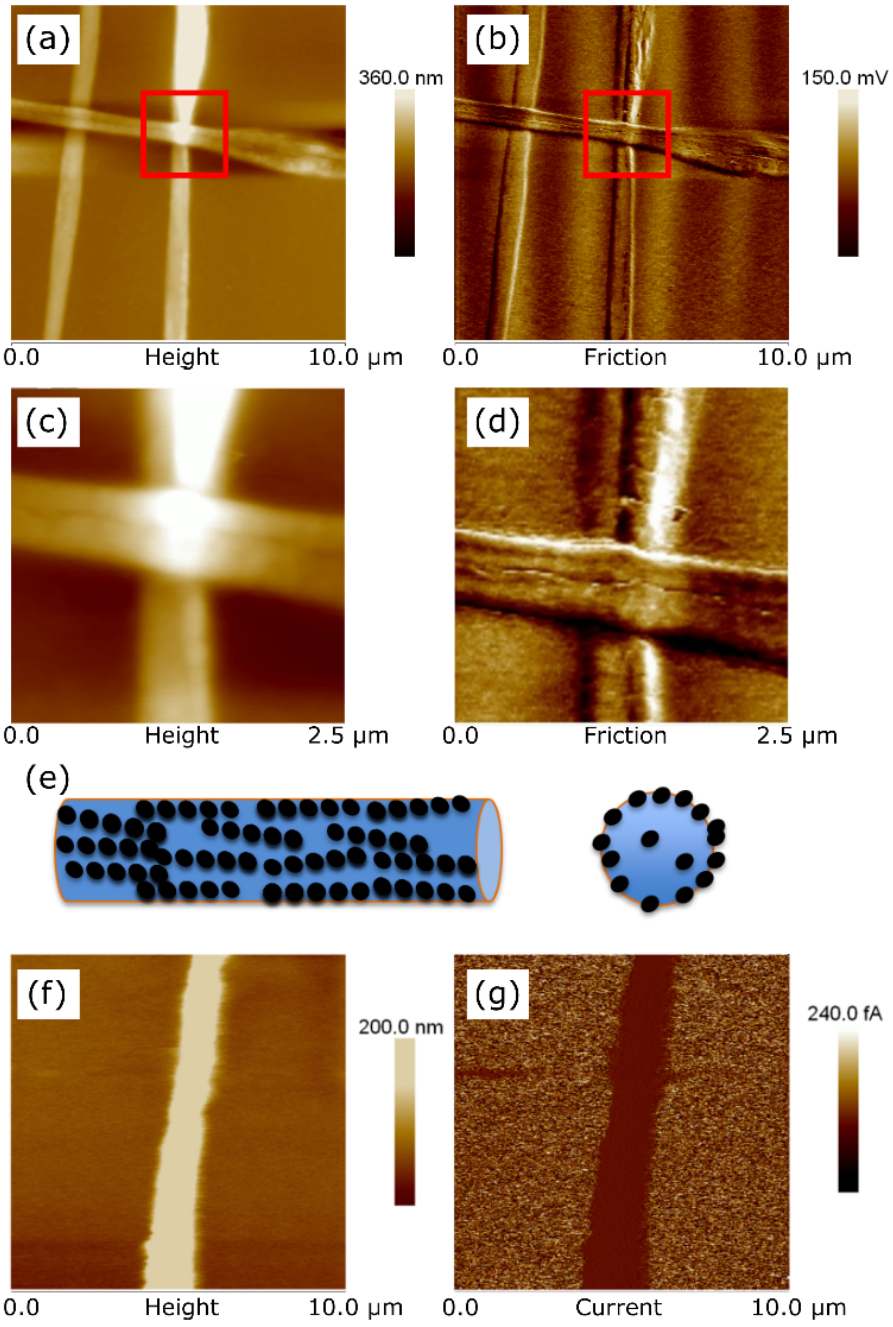

Figure 4. 5 AFM (a) and lateral force (b) micrographs (10 µm ´ 10 µm) of cross-bar MEH-PPV/PVP/PCBM fibers deposited on the blend film with addition of the backfill layer. (c) and (d) are magnified images for the region delineated by red squares in (a) and (b). (e)Schematic presentation of PCBM assembly at the fiber surface. The dark dots represent PCBM nanoparticles. (f, g) TUNA images (10 µm × 10 µm) of ITO-glass/TiO2/ MEH-PPV/PVP/PCBM film/electrospun MEH-PPV/PVP/PCBM fibers samples. (f): Fiber topography and (g) corresponding current map with an applied voltage of 2 V.

The transmission spectra of different samples (MEH-PPV/PVP/PCBM adhesion film, MEH-PPV/PVP/PCBM film with added backfill layer and MEH-PPV/PVP/PCBM film with fibers and backfill layer) are shown in Fig. 4.6 MEH-PPV/PVP/PCBM films exhibit broad absorption at 430-570 nm and maximum absorption at about 490 nm arising from the π-conjugated structure.

Following the addition of the backfill layer, extra peaks at 517 nm and 556 nm and one shoulder at 605 nm are appreciated, correlated to π–π* transitions from P3HT,[56] together with a significant decrease of the transmitted intensity. Research shows that there is no interaction between P3HT and MEH-PPV in terms of absorption spectra and the absorbed energy of the films of the blend series is independent of the blending ratio.[57] Therefore, the here found decrease of transmission through the layer is to be attributed to the incorporation of the nanofibers.

4.3.3 Device Performance and Light Simulation

To elucidate in depth the underlying working mechanisms, the light scattering properties of the ordered fibers embedded in their external medium are described by exploiting the transition matrix (T-matrix) formalism(see Methods). The T-matrix approach combines an accurate description of the scattering process with computational efficiency and a wide particle size range when describing complex non-spherical and composite particles. Here, we model the composite polymer fibers as ordered clusters of spheres,[58]as shown in Fig. 4.7a. In order to mimic the non-spherical fiber section as well as the arrangement of the filaments used in devices we consider ordered arrays of sphere dimers with diameter of 300 nm, as the fiber short axis, and resulting transverse size of each dimer of 600 nm, corresponding to the transverse fiber size. The optical constants of the fibers and of the surrounding medium are calculated using an effective medium theory exploiting the Bruggeman effective dielectric function for composite materials, where the

different composition of the fiber and external medium is accurately taken into account. The Bruggeman effective dielectric function generally applies to a randomly inhomogeneous medium, which is a medium in which no distinguishable inclusions are present. Thus, the effective dielectric function, ϵ_{eff}, for nanofibers or the surrounding medium is calculated separately starting from the dielectric function of their component materials as:

$$\sum_j V_j \frac{\epsilon_j - \epsilon_{eff}}{\epsilon_j + 2\epsilon_{eff}} = 0$$

where V_j is the volume fraction occupied by the different components of dielectric constant ϵ_j.

Light scattering maps for different wavelengths of the incident light, matching different regions of the solar spectrum (from the ultraviolet to the near infrared), are shown in Fig. 4.7b-d. For each wavelength, a map is obtained for the scattered field normalized to an unpolarized incident field intensity, $|E_S/E_0|^2$. From these maps it is clear that the fibrous structures scatter light in an effective way, producing hot spots of radiation spreading across the involved photovoltaic interfaces.

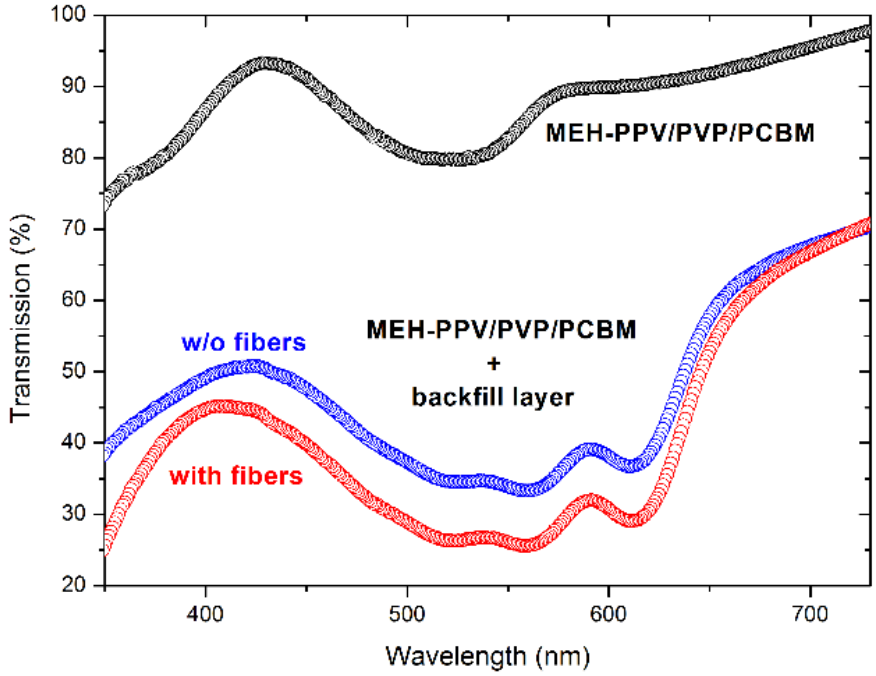

Figure 4. 6 Transmission spectra in the visible and near-infrared, for a MEH-PPV/PVP/PCBM thin film (black circles), a MEH-PPV/PVP/PCBM thin film with backfill layer (blue) and a MEH-PPV/PVP/PCBM thin film with nanofibers and backfill layer (red).

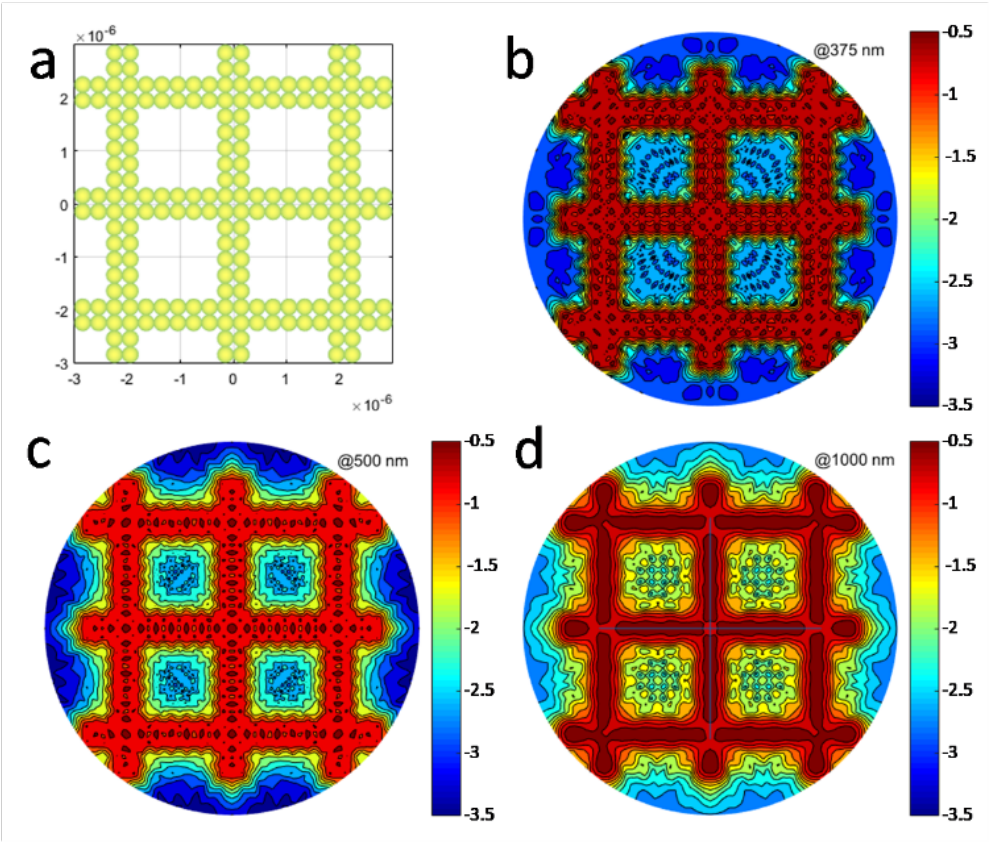

Figure 4. 7 (a) Sketch of the model structure for the light scattering calculations from the ordered, composite polymer nanofiber mats embedded in a dielectric medium.The organic filaments are modeled as aggregate of spheres with 300 nm diameter to match the thickness of the ribbon-shaped fibers realized in the experiments. The optical properties of the nanofibers and of the external medium are obtained using an effective medium theory (see text). (b-d) Normalized intensity maps (|ES/E0|2, in logarithmic scale) of the scattered field for the fiber mats at different wavelentgths: 375 nm (b), 500 nm (c), and 1000 nm (d). In all the calculations the light propagates orthogonally to the fiber mats and with a polarization that is averaged in plane. The fiber structures scatter more strongly in the infrared because of the better-matching average thickness, with scattered light also being more spread out over the structure.

In addition, light scattering is stronger in the near infrared where the average thickness of deposited fibers is closer to the incident wavelength. Moreover, the scattered light at relatively longer wavelengths is spreads out over and outside the fibrous structure, thus reliably increasing optical coupling with the surrounding layer and ultimately photon absorption across the organics.

The performance of thin-film and of fiber-embedding solar cell devices is presented in Table 1, with the corresponding current density-voltage curves shown in Fig. 4.8. With the inclusion of electrospun MEH-PPV/PVP/PCBM fibers into the active layer, the J_{sc} and FF values respectively increase by 0.39 mA cm^{-2} and 4.4% on average, which is indicative of enhanced photon absorption according to the above reported mechanisms and consequently enhanced free-charge generation.[59]No significant change is found for the open-circuit voltage (V_{oc}), suggesting a negligible effect on shunt resistance.Finally, the power conversion efficiency (PCE) is increased by about 20% upon nanofiber embedment (inset of Fig. 4.8). The performance improvement is attributed to the active layer template formed with electrospun nanofibers, which affects various properties of the overall device including the internal light-scattering properties as specified above, in turn enhancing internal absorption of incident photons. In addition, the nanofiber template not only serves as a guide path for electron transport but also increases the interfacial area between donor and acceptor to induce more exciton dissociations. Such template approach is promising in view of application to other polymer solar cell systems in order to achieve higher efficiency under ambient conditions.

	PCE (%)	J_{sc} (mA/cm^2)	V_{oc} (V)	*FF* (%)
W/o fibers	0.853±0.014	3.63±0.34	0.575±0.004	41.1±3.1
With fibers	1.02±0.03	4.02±0.14	0.558±0.03	45.5±0.78

Table 4. 1 Comparison of different device performance (average values).

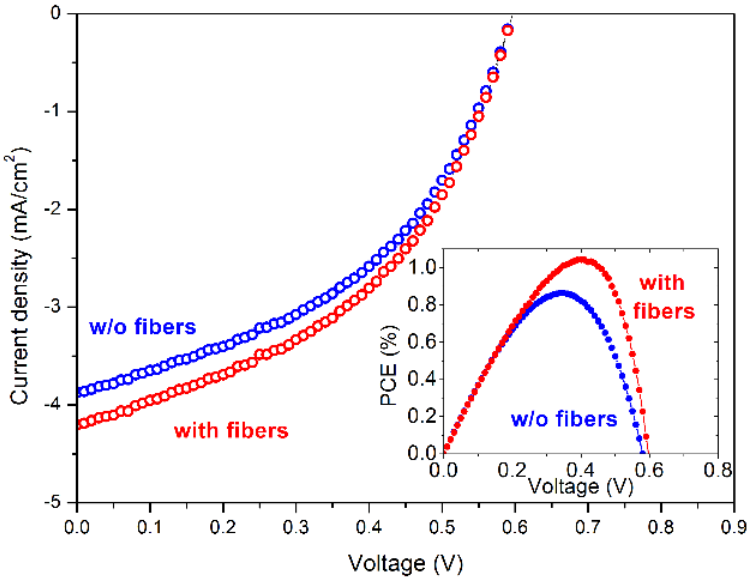

Figure 4. 8 Current density-voltage characteristics for devices with active layers of MEH-PPV/PVP/PCBM film without nanofibers (blue symbols) and with nanofibers (red symbols). Inset: corresponding PCE curves for exemplary devices without (blue symbols) and with nanofibers (red symbols).

4.4. Conclusions

In summary, MEH-PPV/PVP/PCBM nanofibers can be successfully prepared via electrospinning and incorporated into the active layer of polymer solar cell devices. The entangled fiber network serves as a template for the active layer, with effects promoting diffusion and dissociation of photogenerated excitons at involved organic interfaces as well as light-scattering redirecting incident photons across active layers. The electrospinning process forces particle inclusions towards the exterior of the spinning stream. As a result a particle-rich layer is formed with a well-defined pathway for electron conduction, as illustrated in Figure 4.4e. This conformation may be partially responsible for the increased current and fill factor observed when fiber structures are included in BHJ solar cells. The resulting devices are found to exhibit increased J_{sc} and *FF* values compared to thin-film solar cells. A 20% increase is also measured in PCE upon fiber embedment. The here reported performances are largely in line with measurements reported for self-assembled polythiophene nanofibers in PCBM.[18] However, various strategies can be figure out to further improve along these directions. Particularly, electrospun organic nanofibers can be easily doped or decorated by semiconducting quantum dots,[60, 61]which has been found an excellent route to enhance donor-acceptor electronic interaction.[62]Also, electrospinning nanofibers based on conjugated polymer in controlled nitrogen atmosphere might lead to better charge-transport due to the reduced incorporation of oxygen during fabrication.[63] The methodology is likely to be extended to other donor-acceptor material systems, and to flexible solar cell devices as suggested by recent evidences on highly stable bendable field-effect transistors.[64]

References

1. Günes, S.; Neugebauer, H.; Sariciftci, N. S. Conjugated Polymer-Based Organic Solar Cells. *Chem. Rev.* 2007, 107, 1324-1338.

2. Dennler, G.; Scharber, M. C.; Brabec, C. J. Polymer-Fullerene Bulk-Heterojunction Solar Cells. *Adv. Mater.* 2009, 21, 1323-1338.

3. Beaujuge, P. M.; Fréchet, J. M. J. Molecular Design and Ordering Effects in π-Functional Materials for Transistor and Solar Cell Applications. *J. Am. Chem. Soc.* 2011, 133, 20009-20029.

4. Mayer, A. C.; Scully, S. R.; Hardin, B. E.; Rowell, M. W.; McGehee, M. D. Polymer-based solar cells. *Mater. Today* 2007, 10, 28-33.

5. Liu, F.; Gu, Y.; Jung, J. W.; Jo, W. H.; Russell, T. P. On the morphology of polymer-based photovoltaics. *J. Polym. Sci., Part B: Polym. Phys.* 2012, 50, 1018-1044.

6. Chen, W.; Nikiforov, M. P.; Darling, S. B. Morphology characterization in organic and hybrid solar cells. *Energy Environ. Sci.* 2012, 5, 8045-8074.

7. Moulé, A. J.; Meerholz, K. Morphology Control in Solution-Processed Bulk-Heterojunction Solar Cell Mixtures. *Adv. Funct. Mater.* 2009, 19, 3028-3036.

8. Yang, X.; Loos, J.; Veenstra, S. C.; Verhees, W. J. H.; Wienk, M. M.; Kroon, J. M.; Michels, M. A. J.; Janssen, R. A. J. Nanoscale Morphology of High-Performance Polymer Solar Cells. *Nano Lett.* 2005, 5, 579-583.

9. Xin, H.; Reid, O. G.; Ren, G.; Kim, F. S.; Ginger, D. S.; Jenekhe, S. A. Polymer Nanowire/Fullerene Bulk Heterojunction Solar Cells: How Nanostructure Determines Photovoltaic Properties. *ACS Nano* 2010, 4, 1861-1872.

10. Nam, S.; Shin, M.; Kim, H.; Kim, Y. Temperature/time-dependent crystallization of polythiophene:fullerene bulk heterojunction films for polymer solar cells. *Nanoscale* 2010, 2, 2384-2389.

11. Clarke, T. M.; Ballantyne, A. M.; Nelson, J.; Bradley, D. D. C.; Durrant, J. R. Free Energy Control of Charge Photogeneration in Polythiophene/Fullerene Solar Cells: The Influence of Thermal Annealing on P3HT/PCBM Blends. *Adv. Funct. Mater.* 2008, 18, 4029-4035.

12. Wang, H. S.; Lin, L. H.; Chen, S. Y.; Wang, Y. L.; Wei, K. H. Ordered polythiophene/fullerene composite core-shell nanorod arrays for solar cell applications. *Nanotechnology* 2009, 20.

13. Tang, H.; Lu, G.; Li, L.; Li, J.; Wang, Y.; Yang, X. Precise construction of PCBM aggregates for polymer solar cells via multi-step controlled solvent vapor annealing. *J. Mater. Chem.* 2010, 20, 683-688.

14. Jo, J.; Na, S.-I.; Kim, S.-S.; Lee, T.-W.; Chung, Y.; Kang, S.-J.; Vak, D.; Kim, D.-Y. Three-Dimensional Bulk Heterojunction Morphology for Achieving High Internal Quantum Efficiency in Polymer Solar Cells. *Adv. Funct. Mater.* 2009, 19, 2398-2406.

15. Pan, C.; Li, H.; Akgun, B.; Satijia, S. K.; Zhu, Y.; Xu, D.; Ortiz, J.; Gersappe, D.; Rafailovich, M. H. Enhancing the Efficiency of Bulk Heterojunction Solar Cells via Templated Self-Assembly. *Macromolecules* 2013, 46, 1812-1819.

16. Chen, F. C.; Lin, Y. K.; Ko, C. J. Submicron-scale manipulation of phase separation in organic solar cells. *Appl. Phys. Lett.* 2008, 92.

17. Zhao, Y.; Shao, S.; Xie, Z.; Geng, Y.; Wang, L. Effect of Poly (3-hexylthiophene) Nanofibrils on Charge Separation and Transport in Polymer Bulk Heterojunction Photovoltaic Cells. *J. Phys. Chem. C* 2009, 113, 17235-17239.

18. Xin, H.; Kim, F. S.; Jenekhe, S. A. Highly Efficient Solar Cells Based on Poly(3-butylthiophene) Nanowires. *J. Am. Chem. Soc.* 2008, 130, 5424-5425.

19. Xin, H.; Ren, G.; Kim, F. S.; Jenekhe, S. A. Bulk Heterojunction Solar Cells from Poly(3-butylthiophene)/Fullerene Blends: In Situ Self-Assembly of Nanowires, Morphology, Charge Transport, and Photovoltaic Properties. *Chem. Mater.* 2008, 20, 6199-6207.

20. Berson, S.; De Bettignies, R.; Bailly, S.; Guillerez, S. Poly(3-hexylthiophene) Fibers for Photovoltaic Applications. *Adv. Funct. Mater.* 2007, 17, 1377-1384.

21. Reneker, D. H.; Chun, I. Nanometre diameter fibres of polymer, produced by electrospinning. *Nanotechnology* 1996, 7, 216-223.

22. Greiner, A.; Wendorff, J. H. Electrospinning: A Fascinating Method for the Preparation of Ultrathin Fibers. *Angew. Chem. Int. Ed.* 2007, 46, 5670-5703.

23. Persano, L.; Camposeo, A.; Pisignano, D. Active polymer nanofibers for photonics, electronics, energy generation and micromechanics. *Prog. Polym. Sci.* 2015, 43, 48-95.

24. Babel, A.; Li, D.; Xia, Y.; Jenekhe, S. A. Electrospun Nanofibers of Blends of Conjugated Polymers: Morphology, Optical Properties, and Field-Effect Transistors. *Macromolecules* 2005, 38, 4705-4711.

25. Lee, S. W.; Lee, H. J.; Choi, J. H.; Koh, W. G.; Myoung, J. M.; Hur, J. H.; Park, J. J.; Cho, J. H.; Jeong, U. Periodic Array of Polyelectrolyte-Gated Organic Transistors from Electrospun Poly(3-hexylthiophene) Nanofibers. *Nano Lett.* 2010, 10, 347-351.

26. Tu, D. Y.; Pagliara, S.; Camposeo, A.; Persano, L.; Cingolani, R.; Pisignano, D. Single light-emitting polymer nanofiber field-effect transistors. *Nanoscale* 2010, 2, 2217-2222.

27. Liwen, J.; Xiangwu, Z. Fabrication of porous carbon nanofibers and their application as anode materials for rechargeable lithium-ion batteries. *Nanotechnology* 2009, 20, 155705.

28. Chang, C.; Tran, V. H.; Wang, J.; Fuh, Y.-K.; Lin, L. Direct-Write Piezoelectric Polymeric Nanogenerator with High Energy Conversion Efficiency. *Nano Lett.* 2010, 10, 726-731.

29. Persano, L.; Dagdeviren, C.; Maruccio, C.; De Lorenzis, L.; Pisignano, D. Cooperativity in the Enhanced Piezoelectric Response of Polymer Nanowires. *Adv. Mater.* 2014, 26, 7574-7580.

30. Moran-Mirabal, J. M.; Slinker, J. D.; DeFranco, J. A.; Verbridge, S. S.; Ilic, R.; Flores-Torres, S.; Abruña, H.; Malliaras, G. G.; Craighead, H. G. Electrospun Light-Emitting Nanofibers. *Nano Lett.* 2007, 7, 458-463.

31. Vohra, V.; Giovanella, U.; Tubino, R.; Murata, H.; Botta, C. Electroluminescence from Conjugated Polymer Electrospun Nanofibers in Solution Processable Organic Light-Emitting Diodes. *ACS Nano* 2011, 5, 5572-5578.

32. Persano, L.; Camposeo, A.; Carro, P. D.; Fasano, V.; Moffa, M.; Manco, R.; D'Agostino, S.; Pisignano, D. Distributed Feedback Imprinted Electrospun Fiber Lasers. *Adv. Mater.* 2014, 26, 6542-6547.

33. Sundarrajan, S.; Murugan, R.; Nair, A. S.; Ramakrishna, S. Fabrication of P3HT/PCBM solar cloth by electrospinning technique. *Mater. Lett.* 2010, 64, 2369-2372.

34. Burresi, M.; Cortese, L.; Pattelli, L.; Kolle, M.; Vukusic, P.; Wiersma, D. S.; Steiner, U.; Vignolini, S. Bright-White Beetle Scales Optimise Multiple Scattering of Light. *Sci. Rep.* 2014, 4.

35. Kim, T.; Yang, S. J.; Kim, S. K.; Choi, H. S.; Park, C. R. Preparation of PCDTBT nanofibers with a diameter of 20 nm and their application to air-processed organic solar cells. *Nanoscale* 2014, 6, 2847-2854.

36. Bedford, N. M.; Dickerson, M. B.; Drummy, L. F.; Koerner, H.; Singh, K. M.; Vasudev, M. C.; Durstock, M. F.; Naik, R. R.; Steckl, A. J. Nanofiber-Based Bulk-Heterojunction Organic Solar Cells Using Coaxial Electrospinning. *Adv. Energy. Mater.* 2012, 2, 1136-1144.

37. Lee, J.; Ko, H.; Song, E.; Kim, H. G.; Cho, K. Naphthodithiophene-Based Conjugated Polymer with Linear, Planar Backbone Conformation and Strong Intermolecular Packing for Efficient Organic Solar Cells. *ACS Appl. Mater. Interfaces* 2015, 7, 21159-21169.

38. Kim, M.; Jo, S. B.; Park, J. H.; Cho, K. Flexible lateral organic solar cells with core–shell structured organic nanofibers. *Nano Energy* 2015, 18, 97-108.

39. Khanum, K. K.; Ramamurthy, P. C. Instigating network structure in bulk heterojunction organic solar cells creating a unique approach in augmenting the optical absorption. *Polymer* 2016, 91, 146-155.

40. Joly, D.; Jung, J.-W.; Kim, I.-D.; Demadrille, R. Electrospun materials for solar energy conversion: innovations and trends. *J. Mater. Chem. C* 2016, 4, 10173-10197.

41. Greenham, N. C.; Samuel, I. D. W.; Hayes, G. R.; Phillips, R. T.; Kessener, Y. A. R. R.; Moratti, S. C.; Holmes, A. B.; Friend, R. H. Measurement of absolute photoluminescence quantum efficiencies in conjugated polymers. *Chem. Phys. Lett.* 1995, 241, 89-96.

42. Xue, H. L.; Kong, X. Z.; Liu, Z. R.; Liu, C. X.; Zhou, J. R.; Chen, W. Y.; Ruan, S. P.; Xu, Q. TiO2 based metal-semiconductor-metal ultraviolet photodetectors. *Appl. Phys. Lett.* 2007, 90.

43. Mason, M. G. Electronic-Structure of Supported Small Metal-Clusters. *Phys. Rev. B* 1983, 27, 748-762.

44. Borghese, F.; Denti, P.; Saija, R. Scattering from Model Nonspherical Particles Theory and Applications to Environmental Physics. In *Physics of Earth and Space Environments,* [Online] Springer Berlin Heidelberg,: Berlin, Heidelberg, 2003; pp. 1 online resource (xiv, 255 pages). http://dx.doi.org/10.1007/978-3-662-05330-0.

45. Borghese, F.; Denti, P.; Saija, R.; Toscano, G.; Sindoni, O. I. Multiple Electromagnetic Scattering from a Cluster of Spheres. I. Theory. *Aerosol Sci. Technol.* 1984, 3, 227-235.

46. Mackowski, D. W.; Mishchenko, M. I. Calculation of the T matrix and the scattering matrix for ensembles of spheres. *J. Opt. Soc. Am. A* 1996, 13, 2266-2278.

47. Saija, R.; Iati, M. A.; Borghese, F.; Denti, P.; Aiello, S.; Cecchi-Pestellini, C. Beyond Mie theory: The transition matrix approach in interstellar dust modeling. *Astrophys J* 2001, 559, 993-1004.

48. Saija, R.; Iatì, M. A.; Denti, P.; Borghese, F.; Giusto, A.; Sindoni, O. I. Efficient light-scattering calculations for aggregates of large spheres. *Appl. Opt.* 2003, 42, 2785-2793.

49. Borghese, F.; Denti, P.; Saija, R.; Iatì, M. A.; Sindoni, O. I. Optical properties of a dispersion of anisotropic particles with non-randomly distributed orientations. The case of atmospheric ice crystals. *J. Quant. Spectrosc. Radiat. Transfer* 2001, 70, 237-251.

50. Iati, M. A.; Cecchi-Pestellini, C.; Williams, D. A.; Borghese, F.; Denti, P.; Saija, R.; Aiello, S. Porous interstellar grains. *Mon Not R Astron Soc* 2001, 322, 749-756.

51. Yue, G.; Wu, J.; Xiao, Y.; Ye, H.; Lin, J.; Huang, M. Flexible dye-sensitized solar cell based on PCBM/P3HT heterojunction. *Chin. Sci. Bull.* 2011, 56, 325-330.

52. Kratschmer, W.; Lamb, L. D.; Fostiropoulos, K.; Huffman, D. R. Solid C60: a new form of carbon. *Nature* 1990, 347, 354-358.

53. Hwang, I.; Scholes, G. D. Electronic Energy Transfer and Quantum-Coherence in π-Conjugated Polymers. *Chem. Mater.* 2011, 23, 610-620.

54. Camposeo, A.; Pensack, R. D.; Moffa, M.; Fasano, V.; Altamura, D.; Giannini, C.; Pisignano, D.; Scholes, G. D. Anisotropic Conjugated Polymer Chain Conformation Tailors the Energy Migration in Nanofibers. *J. Am. Chem. Soc.* 2016, 138, 15497-15505.

55. Greenfeld, I.; Fezzaa, K.; Rafailovich, M. H.; Zussman, E. Fast X-ray Phase-Contrast Imaging of Electrospinning Polymer Jets: Measurements of Radius, Velocity, and Concentration. *Macromolecules* 2012, 45, 3616-3626.

56. Shrotriya, V.; Ouyang, J.; Tseng, R. J.; Li, G.; Yang, Y. Absorption spectra modification in poly(3-hexylthiophene):methanofullerene blend thin films. *Chem. Phys. Lett.* 2005, 411, 138-143.

57. Ruderer, M. A.; Metwalli, E.; Wang, W.; Kaune, G.; Roth, S. V.; Müller-Buschbaum, P. Thin Films of Photoactive Polymer Blends. *ChemPhysChem* 2009, 10, 664-671.

58. Fazio, B.; Artoni, P.; Antonia Iati, M.; D'Andrea, C.; Lo Faro, M. J.; Del Sorbo, S.; Pirotta, S.; Giuseppe Gucciardi, P.; Musumeci, P.; Salvatore Vasi, C.; Saija, R.; Galli, M.; Priolo, F.; Irrera, A. Strongly enhanced light trapping in a two-dimensional silicon nanowire random fractal array. *Light Sci Appl.* 2016, 5, e16062.

59. Peet, J.; Heeger, A. J.; Bazan, G. C. "Plastic" Solar Cells: Self-Assembly of Bulk Heterojunction Nanomaterials by Spontaneous Phase Separation. *Acc. Chem. Res.* 2009, 42, 1700-1708.

60. Liu, H.; Edel, J. B.; Bellan, L. M.; Craighead, H. G. Electrospun Polymer Nanofibers as Subwavelength Optical Waveguides Incorporating Quantum Dots. *Small* 2006, 2, 495-499.

61. Persano, L.; Camposeo, A.; Di Benedetto, F.; Stabile, R.; Laera, A. M.; Piscopiello, E.; Tapfer, L.; Pisignano, D. CdS–Polymer Nanocomposites and Light-Emitting Fibers by In Situ Electron-Beam Synthesis and Lithography. *Adv. Mater.* 2012, 24, 5320-5326.

62. Ren, S.; Chang, L.-Y.; Lim, S.-K.; Zhao, J.; Smith, M.; Zhao, N.; Bulović, V.; Bawendi, M.; Gradečak, S. Inorganic–Organic Hybrid Solar Cell: Bridging Quantum Dots to Conjugated Polymer Nanowires. *Nano Lett.* 2011, 11, 3998-4002.

63. Fasano, V.; Moffa, M.; Camposeo, A.; Persano, L.; Pisignano, D. Controlled Atmosphere Electrospinning of Organic Nanofibers with Improved Light Emission and Waveguiding Properties. *Macromolecules* 2015, 48, 7803-7809.

64. Manuelli, A.; Persano, L.; Pisignano, D. Flexible organic field-effect transistors based on electrospun conjugated polymer nanofibers with high bending stability. *Org. Electron.* 2014, 15, 1056-1061.